

Published in final edited form as:

Biochemistry. 2013 November 12; 52(45): 7926-7942. doi:10.1021/bi401015t.

# Mössbauer Study and Modeling of Iron Import and Trafficking in Human Jurkat Cells

Nema D. Jhurry<sup>†</sup>, Mrinmoy Chakrabarti<sup>‡</sup>, Sean P. McCormick<sup>‡</sup>, Vishal M. Gohil<sup>†</sup>, and Paul A. Lindahl<sup>\*,†,‡</sup>

<sup>†</sup>Department of Biochemistry and Biophysics, Texas A&M University, College Station, Texas 77843-2128, United States

<sup>‡</sup>Department of Chemistry, Texas A&M University, College Station, Texas 77843-3255, United States

#### **Abstract**

The Fe content of Jurkat cells grown on transferrin-bound iron (TBI) and Fe<sup>III</sup> citrate (FC) was characterized using Mössbauer, EPR, and UV-vis spectroscopies, electron microscopy, and ICP-MS. Isolated mitochondria were similarly characterized. Fe-limited cells contained  $\sim 100 \, \mu M$  of essential Fe, mainly as mitochondrial Fe and non-mitochondrial nonheme high-spin (NHHS) Fe<sup>II</sup>. Fe-replete cells also contained ferritin-bound Fe and Fe<sup>III</sup> oxyhydroxide nanoparticles. Only  $400 \pm$ 100 Fe ions were loaded per ferritin complex, regardless of the growth medium Fe concentration. Ferritin regulation thus appears more complex than is commonly assumed. The magnetic/ structural properties of Jurkat nanoparticles differed from those in yeast mitochondria. They were smaller and may be located in the cytosol. The extent of nanoparticle formation scaled nonlinearly with the concentration of Fe in the medium. Nanoparticle formation was not strongly correlated with ROS damage. Cells could utilize nanoparticle Fe, converting such aggregates into essential Fe forms. Cells grown on galactose rather than glucose respired faster, grew slower, exhibited more ROS damage and generally contained more nanoparticles. Cells grown with TBI rather than FC contained lower Fe concentrations, more ferritin and fewer nanoparticles. Cells in which transferrin receptor expression was increased contained more ferritin Fe. Frataxin-deficient cells contained more nanoparticles than comparable WT cells. Data were analyzed by a chemicallybased mathematical model. Although simple, it captured essential features of Fe import, trafficking and regulation. TBI import was highly regulated but FC import was not. Nanoparticle formation was not regulated but the rate was third-order in cytosolic Fe.

#### **Keywords**

Bioinorganic chemistry; biophysics; chemical kinetics; electronic absorption spectroscopy; electron paramagnetic resonance; ferric (phosphate) oxyhydroxide nanoparticles; ferritin; frataxin; Friedreich's ataxia; inductively coupled plasma mass spectrometry; mathematical modeling; ordinary differential equations; oxidative damage; RNA interference; spectroscopy; transferrin and transferrin receptor

To whom correspondence should be addressed. Phone: 979-845-0956. Fax: 979-845-4719. lindahl@chem.tamu.edu. Supporting Information **Available**. Analytical properties of isolated mitochondria (Table S1), concentrations of reduced hemes *a*, *b*, and *c* in Jurkat cells and isolated mitochondria (Table S2), TEM image of Jurkat cell (Figure S1), a test to distinguish low-loaded ferritin from nanoparticles (Figure S2), X-band EPR spectra of Jurkat cells (Figure S3), EPR spectra of isolated mitochondria (Figure S4), UV-Vis spectra of whole Jurkat cells (Figure S5), UV-Vis spectra of isolated mitochondria (Figure S6), Oxyblot analysis of cells grown under different conditions (Figure S7), Western blot indicating overexpression of TfRC (Figure S8), Western blot indicating knockdown of frataxin (Figure S9), UV-Vis of frataxin-deficient cells vs. normal cells (Figure S10), and Uncertainties in model parameters (Table S3). This material is available free of charge via the Internet at http://pubs.acs.org.

Iron is essential in human metabolism due to its extensive redox, substrate binding, and catalytic properties. This transition metal is found in various forms, including hemes, Fe/S clusters, and nonheme mononuclear and binuclear centers. Conversely, excess Fe is widely regarded to be toxic to cells because it can generate Reactive Oxygen Species (ROS) through the Fenton reaction. Hence, Fe import, trafficking, utilization and storage must be tightly regulated by cells. <sup>2, 3</sup>

Mammalian cells import Fe through many pathways, the best studied of which involves transferrin, a blood plasma protein that coordinates two Fe<sup>III</sup> ions.<sup>4</sup> The cell-surface transferrin receptor TfRC1 mediates the endocytic import of transferrin-bound iron (TBI). This is followed by acidification of the endosome, release of Fe<sup>III</sup> from transferrin, reduction to Fe<sup>II</sup> and export of Fe<sup>II</sup> from the endosome to the cytosol via the divalent metal transporter DMT1.<sup>5</sup> Expression of the transferrin receptor (TfRC1) is regulated post-transcriptionally by the iron regulatory proteins IRP1 and IRP2.<sup>6</sup> Both bind to and stabilize the 3'-UTR of TfRC1 mRNA under iron-deficient conditions. This promotes TfRC1 translation and thus Fe import via the TBI pathway.<sup>6</sup>

IRP1/2 also regulate the concentration of ferritin in the cell. Ferritin is a spherical 24-subunit protein complex used by the cell to store Fe. It has a hollow 7 nm-diameter core that can store up to  $\sim 4500~{\rm Fe^{III}}$  ions as an oxyhydroxide aggregate. When cells are iron deficient, IRP1/2 bind to the 5′-UTR of ferritin mRNA. This prevents mRNA translation, and leads to a decline of ferritin expression. When cells are Fe replete, IRP1/2 do not bind ferritin mRNA which increases ferritin expression, allowing storage of excess cellular Fe.  $^6$ 

Other Fe import pathways are less well defined, and are often referred to as a single pathway in which non-transferrin-bound iron (NTBI) is imported. Fe<sup>III</sup> citrate (FC) is a likely component of NTBI. Although many important aspects of NTBI and its import pathways are known, much remains to be learned regarding their role in cellular physiology. A cell-surface ferrireductase is required for the reduction of NTBI Fe<sup>III</sup> to Fe<sup>II</sup> prior to uptake. Cell-surface metal transporters such as DMT1, 2 the zinc transporter ZIP 14, 3 Dcytb and L-type calcium channels 4 may be involved. NTBI may also be imported via bulk/adsorptive endocytosis.

Although incompletely defined, NTBI plays important roles in a number of diseases. NTBI is found in the blood plasma of patients with Fe-overload diseases such as  $\beta$ -thalassemia, <sup>16</sup> idiopathic hemochromatosis, <sup>17</sup> hypotransferrinemia, <sup>18</sup> and hereditary hemochromatosis. <sup>19</sup> This typically leads to iron accumulation in the liver and/or spleen. NTBI has also been implicated in the pathology of Alzheimer's disease. <sup>20</sup> NTBI uptake is not as tightly controlled as that of TBI, consistent with a role in cellular Fe overload and Fe-induced toxicity. <sup>8</sup> Hepatocytes import NTBI > 20-fold faster than they import TBI, <sup>21</sup> which explains why NTBI is cleared efficiently from the blood by the liver. <sup>22</sup> Growth of cells on NTBI leads to severe Fe overload and oxidative damage. <sup>23-25</sup>

Few studies have probed Fe metabolism in human cells using iron-centric methods such as Mössbauer (MB) spectroscopy. This technique, used in conjunction with EPR and other biophysical methods (e.g. UV-vis and EM), can effectively evaluate the speciation of Fe in cells,  $^{26\text{-}28}$  including human Jurkat cells grown in medium containing 10  $\mu$ M FC.  $^{28}$  The majority of Fe in these Fe-replete cells is bound to ferritin. Also evident are [Fe<sub>4</sub>S<sub>4</sub>] clusters and heme centers primarily associated with mitochondrial respiratory complexes, and Fe<sup>III</sup> oxyhydroxide nanoparticles that exhibit superparamagnetic behavior.  $^{28}$  In low-temperature low-field MB spectra, the nanoparticles exhibited a broad quadrupole doublet with  $\delta=0.48$  mm/s,  $\Delta E_{O}=0.57$  mm/s.

Whitnall et~al. recently used MB spectroscopy to identify nonferritin mitochondrial Fe deposits in a mouse model of Friedreich's ataxia. Friedrich's ataxia is the most common autosomal recessive ataxia; it causes progressive degeneration of the nervous system and heart. The deposits observed in heart tissue exhibit a broad quadrupole doublet in low-temperature low-field MB spectra. The associated parameters ( $\delta=0.48$  mm/s,  $\Delta E_Q=0.71$  mm/s) are similar to those observed in Jurkat cells. The mice had a muscle creatine kinase conditional knockout of frataxin, a mitochondrial matrix protein involved in Fe/S cluster biosynthesis. Yeast lacking the frataxin homolog (Yfh1p) accumulate massive amounts of Fe<sup>III</sup> phosphate oxyhydroxide nanoparticles in their mitochondria, along with a deficiency of Fe/S clusters and heme centers.

Here, we report how the cellular concentrations of such Fe-containing species in human Jurkat cells vary with the concentration of FC and TBI in the growth medium. We examined the effect of different carbon sources (glucose *vs.* galactose) on the Fe content of these cells, and the effect of altering the expression levels of the transferrin receptor and frataxin. A mathematical model defining the fate of Fe that enters the cell as TBI and FC was developed.

# **Experimental Procedures**

#### Cell culture

Cells were grown in a 24 L custom-designed all-glass bioreactor. <sup>28</sup> Cells were counted and viability evaluated as described.<sup>28</sup> Glucose-free RPMI 1640 custom-formulated powder (Gemini Bio-Products, West Sacramento, CA) was reconstituted in distilled deionized water as per manufacturer's instructions, and supplemented with glucose or galactose (10 mM final concentration). The medium was supplemented with <sup>57</sup>Fe<sup>III</sup> citrate (<sup>57</sup>FC) to 3, 10, and 30 μM final concentrations. Aqueous <sup>57</sup>Fe<sup>III</sup> was obtained by dissolving <sup>57</sup>Fe metal (Isoflex USA) in a 1:1 mixture of trace-metal-grade HNO<sub>3</sub> and HCl. The solution was diluted to a concentration of 80 mM <sup>57</sup>Fe with double-distilled deionized (DDDI) H<sub>2</sub>O to prepare a stock solution of <sup>57</sup>Fe. <sup>57</sup>FC was prepared by mixing the stock solution with DDDI H<sub>2</sub>O, and a 4:1 molar ratio of sodium citrate dihydrate: <sup>57</sup>Fe. The pH of the solution was adjusted to 5.0, and the volume was adjusted with DDDI H<sub>2</sub>O to a final concentration of 40 mM <sup>57</sup>FC. Enriched diferric transferrin (<sup>57</sup>TBI) was prepared as described. <sup>32</sup> Apotransferrin (Lee Biosolutions, St. Louis, MO) was dissolved at 10 mg/mL in phosphatebuffered saline (PBS, pH 7.4) containing 0.01 M NaHCO<sub>3</sub>. Four molar equivalents of <sup>57</sup>FC were added per mol of apo-transferrin. After 4 hr at RT, the solution was centrifuged through a 20 kD MW cut-off membrane (Amicon Ultra 15 mL Concentrator). The <sup>57</sup>TBIcontaining retentate (~1 mL) was washed twice with 10 mL of PBS buffer containing 0.01 M NaHCO<sub>3</sub>, spun through the 20 kD cut-off membrane and re-suspended in PBS buffer (Phosphate Buffered Saline, pH 7.4) at a concentration of 10 mg/mL. This <sup>57</sup>TBI stock was added to the cell culture medium to 3, 10, and 30 µM final concentrations. Whole-cell MB and EPR samples were prepared as described.<sup>28</sup>

#### Total RNA isolation and cDNA synthesis

Total RNA was extracted from Jurkat cells using the hot-phenol method. <sup>27</sup> Cells were grown to maximum density ( $\sim 2.5 \times 10^6$  cells/mL) in 200 mL of culture medium and harvested by centrifugation at 700×g for 5 min. Cells were washed twice with PBS buffer, re-suspended in 2 mL of AE buffer (50 mM sodium acetate, pH 5.3, 10 mM EDTA) and lysed by adding SDS (1% w/v, final concentration). An equal volume of AE-saturated phenol was added to the cell lysate. The mixture was incubated at 65°C for 10 min and vortexed every 2 min. The mixture was chilled rapidly in liquid N<sub>2</sub> and spun at 4000×g for 5 min (Beckman Coulter) to separate the phases. The aqueous phase was collected, mixed

thoroughly with an equal volume of a 25:24:1 volume-ratio solution of phenol:chloroform:isoamyl alcohol, and spun at  $4000\times g$ . The aqueous phase was collected and mixed with 0.1 volumes of 3 M sodium acetate and 2.5 volumes of pure ethanol. The solution was spun at 6400 rpm on a Qualitron DW-41 microcentrifuge for 5 min. The RNA-containing pellet was washed 3× with 80% ethanol, air-dried for 1 hr and re-suspended in 200  $\mu L$  of TE buffer (10 mM Tris, pH 7.5, 1 mM EDTA). Contaminating DNA was removed using the DNA-Free reagent kit (Ambion) as per manufacturer's instructions. cDNA was synthesized from RNA using the Super-Script Vilo cDNA synthesis kit (Applied Biosystems) as per manufacturer's instructions.

#### TfRC1 overexpression

Primers for cDNA amplification of the ORF of the TfRC1 gene werecustom-designed (Life Technologies: forward primer: 5'- CACC ATGATGGATCAAGCTAGATCAGC-3'; reverse primer: 5'- TTAAAACTCATTGTCAATGTCCCA-3'). Underlined nucleotides were added to the 5' end of the forward primer to enable directional cloning into the pcDNA 3.1 vector (Life Technologies). The TfRC1 gene was amplified from the cDNA using Accuprime Supermix (Life Technologies), along with 300 nM of the forward and reverse primers, as per manufacturer's instructions. PCR product size was determined by electrophoresis at 50 V using a 0.7% agarose gel and visualized using SYBR Green Fluorescent dye. The PCRproduct was sequenced using 3 sets of forward and reverse primers that were complementary to 3 adjacent 800 bp regions of the TfRC1 cDNA ORF sequence. Each 800 bp region was amplified via sequencing PCR, using the BigDye Terminator mix (Life Technologies) as per manufacturer's instructions. PCR products were sequenced and analyzed on an ABI PRISM 3100 Genetic Analyzer. The TfRC1 PCR product was directionally cloned into pcDNA 3.1 vector as per manufacturer's instructions (Life Technologies). The resulting plasmid was transformed into OneShot TOP10 E. coli competent cells (Life Technologies), which were then plated and grown at 37 °C overnight on LB agar plates containing 100 µg/mL of ampicillin. A colony was picked from the plate and grown overnight in liquid LB containing 100 µg/mL of ampicillin. Plasmids were purified from these E. coli cells using the PureLink Quick Plasmid Miniprep kit (Life Technologies) as per manufacturer's instructions. The insertion of the TfRC1 gene into the plasmid was verified by performing PCR on the isolated plasmid using the forward and reverse primers (T7 forward and BGH reverse) provided with the pcDNA 3.1 Directional TOPO expression kit (Life Technologies). The sequence of the product cloned into the isolated plasmid was verified as described above.

TREx Jurkat cells were transfected with the TfRC1 plasmid using Lipofectamine 2000 (Life Technologies) as per manufacturer's instructions. Transfected cells were selected by growth for 2 wks on medium containing  $1000~\mu g/mL$  geneticin. TfRC1 overexpression was verified by Western Blot, using a rabbit anti-TfRC1 primary antibody (Santa Cruz Biotechnology) and an HRP-conjugated anti-rabbit secondary antibody (Life Technologies).

For the iron starvation experiment, cells were first grown in 500 mL of medium to a density of  $2\times10^6$  cells per mL, then spun down and washed once with sterile PBS containing 1 mM EGTA, and then suspended in neat sterile PBS buffer. The cells were spun down again, and resuspended in complete unsupplemented medium containing 100  $\mu$ M desferrioxamine for 12 hr. The cells were pelleted again, washed with sterile neat PBS buffer, and resuspended again in 1500 mL of complete growth medium supplemented with 3  $\mu$ M  $^{57}$ TBI. Cells were grown to a maximum density of  $3\times10^6$  cells per mL, and a MB sample was prepared as described.  $^{28}$ 

#### Mitochondria isolation

Mitochondria were isolated anaerobically from cells grown with 3 and 30  $\mu$ M FC, as well as from cells grown with 1.5  $\mu$ M diferric transferrin (i.e. 3  $\mu$ M TBI) as described. <sup>28</sup> Freshly harvested cells were imported into an Ar-atmosphere glove box (MBraun, Labmaster, with < 10 ppm O<sub>2</sub>). They were washed twice with PBS buffer (pH 7.4), then re-suspended in degassed Mitochondria Isolation Buffer (MIB: 225 mM D-mannitol, 75 mM sucrose, 5 mM HEPES, 1 mM EGTA and 1 mM PMSF, pH 7.4). The cell suspension was subjected to N<sub>2</sub>-cavitation at 800 psi for 15-20 min using a disruption vessel (model 4635, Parr instruments). The cavitation extract was centrifuged at 800×g for 10 min. The resulting supernatant was centrifuged at 9000×g for 30 min. The pellet was re-suspended in MIB buffer and the resulting solution was layered over a discontinuous gradient of 7.5 mL of 6% Percoll: 3 mL of 17% Histodenz: 3 mL of 35% Histodenz in MIB as described. <sup>33</sup> The gradients were centrifuged at 45000×g for 1 hr. Mitochondria were collected at the 17:35% interface, washed once with MIB, packed into MB cups or EPR tubes at 9000×g, frozen and stored in liquid N<sub>2</sub>.

#### **Quantitative Western blots**

Whole cell samples were packed into EPR tubes and diluted by a known volume of cell lysis buffer (0.1 M Tris-HCl buffer (pH 7.4) containing 1% Triton X-100 and 1 mM PMSF). Protein concentrations were determined using the BCA Protein Assay kit (Thermo Scientific Pierce Protein Research Products). Various known amounts of human holo-ferritin (Lee Biosolutions, St. Louis, MO) were loaded and separated on a 7.5% polyacrylamide native gel, along with 20 µL of cell lysates from cells grown in glucose or galactose-containing medium supplemented with 3  $\mu M,\,10~\mu M,$  or 30  $\mu M$  of either FC or TBI. Proteins were transferred to Immun-Blot PVDF membranes (Bio-Rad) overnight at 40 V. Membranes were treated for 2 hr with Blocker casein solution (Thermo Scientific), then incubated for 1 hr with rabbit polyclonal primary antibody specific to mammalian ferritin (Abnova) diluted 1:200 in Blocker casein solution. Membranes were then incubated with goat anti-rabbit HRP conjugated secondary antibody (Life Technologies) diluted 1:3000 in Blocker casein solution, followed by detection using the Thermo Scientific Enhanced Chemiluminescent Western Blotting substrate. Images were acquired using the FujiFilm LAS-4000 mini imager. Ferritin bands were analyzed using MultiGauge software. A calibration curve was generated using the intensities of the human holo-ferritin bands. Ferritin concentrations of various cell lysates were quantified in terms of absolute cellular concentrations by accounting for the dilution factors and employing the packing efficiency of Jurkat cells that was determined previously.<sup>28</sup>

#### **Biophysical studies**

EPR spectra of whole cells and isolated mitochondria were acquired using an X-band EMX spectrometer (Bruker Biospin Corp., Billerica, MA) equipped with an Oxford Instruments ER900A cryostat. Spin quantifications were performed with SpinCount (http://www.chem.cmu.edu/groups/hendrich/facilities/index.html), using 1.00 mM CuSO<sub>4</sub>-EDTA as a standard. MB spectra were collected on a model MS4 WRC spectrometer and a model LHe6T spectrometer, capable of generating 0-6 T fields (SEE Co., Edina, MN). Both instruments were calibrated using the spectrum of  $\alpha$ -Fe foil collected at room temperature.

For UV-visible spectroscopy, packed whole cell and mitochondrial samples from EPR tubes were diluted 2-fold with PBS buffer and MIB buffer respectively in the glove box. They were placed in a custom 2 mm pathlength quartz UV-vis cuvette (Precision cells), sealed with a rubber septum and removed from the box. Spectra were collected on a Hitachi U3310 spectrometer with a Head-on photomultiplier tube. Heme signals were simulated using OriginPro as described.<sup>34</sup>

# Ferritin loading with Fe<sup>ll</sup> sulfate in whole-cell lysates

After collecting MB spectra of Jurkat cells grown with 30  $\mu$ M  $^{57}FC$ , the sample was thawed at RT and re-suspended homogenously in an equal volume of non-denaturing cell lysis buffer containing 1 mM of PMSF. The lysate was split into two; to half was added  $^{56}Fe^{II}$  sulfate in aqueous solution to a final concentration of  $\sim 6.25$  mM; the other half was left untreated. Both samples were exposed to air and mixed regularly for 2 hr. Each sample was placed in a 3 mL MB cup and frozen immediately in liquid  $N_2$ .

# **Electron microscopy and EDX imaging**

Cells were pelleted at  $700\times g$  for 10 min and washed 3 times with RPMI 1640 medium. Cells were fixed overnight with acrolein vapor, dehydrated for 2 days with ethylene glycol, infiltrated and embedded in epoxy resin by polymerization at  $60\,^{\circ}\text{C}$  overnight. Ultrathin sections were obtained using an Ultracut E microtome (Reichert-Jung). Sections were carbon-stabilized overnight. Elemental analysis was performed on a TECNAI F20 Twin (scanning) transmission electron microscope ((S)TEM) fitted with a Schottky field emission gun, a high-angle-annular-dark-field (HAADF) detector, and an Oxford instruments ultrathin window energy-dispersive-x-ray spectroscopy (EDX) detector. EDX spectra were collected at a  $\sim 15^{\circ}$  tilt angle with a stationary electron probe in STEM mode. The STEM was operated at a  $200\,\text{kV}$  accelerating voltage. Spectral images were obtained from areas of interest by the electron-microscope-spectroscopy system. Elemental maps were acquired after choosing proper energy windows for element-specific transitions along with STEM-HAADF images.

#### **Extracellular Flux Measurements**

Cells were grown in RPMI 1640 medium containing 10 mM glucose or galactose, 5% Newborn Calf Serum (Invitrogen), 10 μM FC, 100 units/L penicillin, 100 μg/L streptomycin, and 0.25 µg/L amphotericin B. Cells were spun at 700g for 5 min and the pellet was washed with PBS buffer (pH 7.4). Cells were re-suspended in Modified DMEM XF Assay medium (Seahorse Biosciences, Billerica, MA) supplemented with either 10 mM glucose or 10 mM galactose. Cell-Tak™ (BD Biosciences), a cell and tissue adhesive, was diluted in 0.1 M sodium bicarbonate buffer (pH 8.0) as per manufacturer's instructions and used to coat the wells of a 24-well plate (Seahorse) by adding  $\sim$ 4 µg of Cell-Tak<sup>TM</sup> in a total volume of 50 μL per well. O<sub>2</sub> consumption (OCR) and extracellular acidification rates (ECAR) were measured on the Extracellular Flux Analyzer (XF24) (Seahorse Biosciences) as described<sup>35</sup> with minor modifications. Briefly, Jurkat cells were seeded in Cell-Tak<sup>TM</sup> treated XF24-well cell culture microplates at 250,000 cells/well in 10 mM glucose- or 10 mM galactose-containing XF assay media and incubated at 37°C for ~1 hr prior to measurements. The baseline was measured 3 times prior to adding oligomycin (1 µM final concentration); the data presented here represent the third measurement. Each measurement included a mix (2 min), wait (3 min) and measure (2 min) cycle.

#### **Oxyblot Assays**

Whole-cell lysates were prepared in cell lysis buffer (0.1 M Tris-HCl, 1% Triton X-100, 1 mM PMSF). Twenty  $\mu g$  of cellular protein from each extract was solubilized with 10% w/v SDS, derivatized with 2,4-dinitrophenylhydrazine (DNPH) and loaded onto a 12% SDS-PAGE gel. Oxyblot analysis was performed using the DNPH-primary antibody and the HRP-conjugated secondary antibody provided with the manufacturer's kit (Millipore).

#### **ICP-MS**

Packed whole cells and mitochondrial samples from EPR tubes were diluted with a known volume of PBS buffer and MIB buffer respectively. Suspensions were digested overnight

with concentrated trace-metal-grade nitric acid (final concentration 20-30%) in 15 mL plastic screw-top tubes (BD Falcon). Digested samples were diluted with 4 mL of double-distilled and deionized water. Metal concentrations were measured in  $\rm H_2$  and He collision modes using ICP-MS (Agilent Technologies model 7700×). The absolute metal concentrations in the samples were obtained by adjusting for dilution factors and packing efficiencies, and then averaging individual numbers.

#### Frataxin knockdown

Frataxin protein knockdown was performed using the BLOCK-iT Inducible H1 RNAi Entry Vector kit (Life Technologies) as per manufacturer's instructions. Four DNA oligonucleotide sequences encoding shRNA sequences specific to frataxin mRNA were designed using Life Technologies' BLOCK-iTTM RNAi Designer (rnaidesigner.invitrogen.com/rnaiexpress/) and cloned into pENTR<sup>TM</sup>/H1/TO vector (Life Technologies). The plasmids were separately transformed into One Shot® TOP10 chemically competent E. coli cells, which were plated and selected on LB agar plates with 50 μg/mL kanamycin. Bacterial colonies were picked and grown in liquid LB with 50 μg/ mL kanamycin. Plasmids were purified from the liquid cultures using PureLink<sup>TM</sup> HQ Mini Plasmid Purification kit (Life Technologies) as per manufacturer's instructions. Plasmids were transfected into Jurkat cells using Xfect<sup>TM</sup> transfection reagent (Clontech) as per manufacturer's instructions. Cells were grown under selection for 2-3 weeks in RPMI-1640 medium supplemented with tetracycline-negative fetal bovine serum (PAA Laboratories), 10 μg/mL blasticidin, and 50 μg/mL Zeocin. After selection, frataxin knockdown was induced by adding tetracycline to a final concentration of 3 µg/mL in the cultures. Transfected cells were allowed to grow in the presence of tetracycline for 4-5 days before being assayed for frataxin knockdown.

To assay for frataxin knockdown, transfected cells (both uninduced and induced) were grown to a maximum density of 2×10<sup>6</sup> cells/mL. Cells were spun down, washed with PBS buffer, and lysed using ice-cold RIPA buffer (RadioImmunoprecipitation Assay Buffer: 50 mM Tris HCl, 150 mM NaCl, 1% Triton X-100, 0.5% sodium deoxycholate, 0.1% SDS, pH 8.0). Protein concentrations of cell lysates were determined using Pierce BCA Protein Assay Kit (Thermo Fisher Scientific) as per manufacturer's instructions. Forty μg of protein was boiled with denaturing Laemmli buffer and loaded on a 10% polyacrylamide gel. SDS-PAGE was carried out at 100 V, and proteins were transferred to Immunblot-PVDF membranes for 16 hr at 20 V. Membranes were blocked for 2 hr using Blocker Casein solution (Thermo Fisher Scientific). Membranes were then incubated (with shaking) in rabbit polyclonal anti-frataxin primary antibody (Abcam) diluted 1:500 in PBS buffer. Membranes were subsequently rinsed 3× with PBS buffer, and incubated with goat antirabbit HRP conjugated secondary antibody diluted 1:3000 in PBS buffer. Membranes were again rinsed 3× with PBS buffer, and immersed in Pierce ECL Western Blotting substrate (Thermo Fisher Scientific). Frataxin bands were detected using FujiFilm LAS-4000 mini imager. The frataxin band intensities were analyzed by densitometry using ImageJ software. The DNA oligonucleotide encoding the shRNA sequence 5'-GGACTATGATGTCTCTTTGGCGAACCAAAGGAGACATCATA-3' (loop region indicated in bold), which targets bases 583-603 of frataxin mRNA, resulted in 50%-70%

indicated in bold), which targets bases 583-603 of frataxin mRNA, resulted in 50%-70% knockdown of frataxin protein after 4-5 days of induction by tetracycline, as judged by densitometry analysis of frataxin bands. The remaining shRNA sequences tested did not result in measurable frataxin knockdown. Therefore, the cells expressing the shRNA targeted to bases 583-603 were chosen for further analysis.

For spectroscopic investigations, transfected cells expressing shRNA targeted to frataxin were grown up to 3 L in complete RPMI-1640 medium supplemented with 50  $\mu g/mL$ 

Zeocin, and 10  $\mu$ g/mL tetracycline to ensure continuous frataxin knockdown. <sup>57</sup>FC was added to a final concentration of 10  $\mu$ M to the cell culture. Cells were washed with PBS containing 1 mM EGTA, followed by PBS without EGTA, packed into MB cups, and frozen in liquid N<sub>2</sub>. After MB analysis, cells were thawed and analyzed by UV-Vis spectroscopy and ICP-MS as described before. WT cells grown with 10  $\mu$ M <sup>57</sup>FC were analyzed alongside the transfected cells for comparison.

### Results

In this study, we use biophysical spectroscopy to characterize the iron content of human Jurkat cells grown under different conditions and when genetically modified in different ways. For ease of discussion, we introduce the nomenclature #AB to describe the investigated states of WT cells. Accordingly, "#" indicates the concentration of Fe supplementing the growth medium, with possible values of 0, 3, 10, 30 or 100  $\mu M$ . "A" indicates whether the supplemented Fe was TBI (A = T) or FC (A = F). "B" indicates whether the medium used glucose (B = U) or galactose (B = L) as the carbon source. For example, "3FU" refers to cells grown on glucose-containing medium supplemented with 3  $\mu M$  ferric citrate.

#### Iron Content of 3FU cells

To evaluate the essential Fe content of human cells, we prepared cells under Fe-limited conditions. However, the concentration of natural abundance endogenous Fe in the medium was substantial ( $\sim 6\,\mu M^{28}$ ). Unlike yeast cells that can be grown in chemically-defined minimal synthetic medium, human cells require fetal bovine or newborn calf serum which contains significant amounts of Fe. Grown in such unsupplemented medium, Jurkat cells contained  $100\pm20\,\mu M$  of Fe. These cells grew at about the same rate as in medium supplemented with  $3-30\,\mu M$   $^{57}FC$ , namely with a doubling time (DT) of 24 hr. This indicates that growth was not limited by the endogenous Fe content of the unsupplemented medium.

We attempted to reduce the concentration of endogenous Fe by adding (in different batches) desferrioxamine (DFO) and bathophenanthroline sulfonate (BPS), well-known chelators of Fe<sup>III</sup> and Fe<sup>II</sup> ions, respectively. Similar procedures have been used to create Fe-deficient conditions in yeast.  $^{26}$  However, Jurkat cells did not grow in the presence of 100  $\mu M$  DFO or BPS, which disallowed further analysis of cells subjected to Fe-deficient conditions.

For MB studies, we grew cells in medium supplemented with as little as 3  $\mu$ M <sup>57</sup>FC. Although not strictly Fe-deficient, this Fe concentration was significantly lower than used in our previous investigation. <sup>28</sup> The 5 K 0.05 T MB spectra of 3FU cells (Figure 1A) was dominated by a sextet which collapsed into a doublet at 70 K (Figure 1B). This behavior and the apparent hyperfine splitting of the sextet ( $H_{\rm eff}$  = 480 kG) and MB parameters for the resulting doublet ( $\delta$  = 0.55 mm/s,  $\Delta E_Q$  = 0.25 mm/s) are typical of ferritin. We have assigned this feature as such (see Table 1 for a list of Fe-containing species found in these cells). Fe-bound ferritin represented about half of the Fe in the sample (52% of 220  $\mu$ M = 114  $\mu$ M). Assuming that this storage form of Fe is unnecessary for cellular metabolism, the remaining  $\sim$  100  $\mu$ M Fe in these cells matches the concentration of Fe in cells grown on unsupplemented medium. We suggest that *Jurkat cells require*  $\sim$  100  $\mu$ M cellular Fe for normal growth; this is the concentration of essential Fe in these cells.

The non-ferritin forms of Fe evident in the spectra of 3FU cells included the central doublet (CD) and non-heme high-spin (NHHS) Fe<sup>II</sup> doublet. The CD primarily includes the S=0 [Fe<sub>4</sub>S<sub>4</sub>]<sup>2+</sup> clusters and LS Fe<sup>II</sup> hemes found in mitochondrial respiratory complexes. This doublet represented  $\sim 25\%$  of the intensity (55  $\mu$ M) of the 5 K low-field MB spectrum of

Figure 1A. At 70 K the ferritin sextet collapsed, revealing the high-energy line of a NHHS Fe<sup>II</sup> doublet (simulated by the green line in Figure 1B). The NHHS Fe<sup>II</sup> doublet represented 13% of spectral intensity, which corresponds to *ca.* 30  $\mu$ M Fe<sup>II</sup> ions. The observed spectral parameters ( $\delta$ = 1.3 mm/s,  $\Delta E_Q$  = 3.0 mm/s) are typical of Fe<sup>II</sup> ions coordinated primarily by 0 and N ligands. These two species (the CD and NHHS Fe<sup>II</sup>) represent the majority of the essential Fe in Jurkat cells. Interestingly, Fe-deficient yeast cells which also contained only essential Fe exhibited significant contributions from the same two components.<sup>26</sup> Although the function of the NHHS Fe<sup>II</sup> ions in yeast has not been established, most of it was not located in mitochondria.

The concentration of the ferritin protein complex in 3FU cells was determined by quantitative Western blotting (Figure 2, Table 1) to be 0.3  $\mu$ M, indicating an average of 400 Fe atoms per ferritin complex (114  $\mu$ M Fe/0.3  $\mu$ M ferritin). Populations of purified ferritin complexes afford binomial-like Fe-loading distributions, <sup>36, 37</sup> and we interpret our results similarly for *in vivo* ferritin populations.

We isolated mitochondria from 3FU cells. The Fe concentration of the organelle was low (280  $\mu$ M, Table S1) compared to mitochondria isolated from 10FU cells. <sup>28</sup> Also, the corresponding 5 K low-field MB spectrum (Figure 1C) was weak. Nevertheless, the CD doublet clearly dominated the spectrum, corresponding to at least half of the total intensity. The degree of resolution between the two legs of the CD indicated that the level of Fe<sup>III</sup> nanoparticles in the sample was low. HS Fe<sup>II</sup> heme and NHHS Fe<sup>II</sup> species contribute quadrupole doublets with well-defined  $\delta$  and  $\Delta E_Q$  values. Such doublets at ca. 5% intensity for each can be fitted easily in the spectrum of Figure 1C (this is not conclusive evidence that such material is present, given the noise). Isolated mitochondria did not exhibit significant levels of a ferritin-like sextet. A minor ferritin-like feature could be distinguished from the baseline, but whether it arose from mitochondrial ferritin or a contaminant of cytosolic ferritin could not be determined (we suspect the latter).

The lack of a significant NHHS  $Fe^{II}$  doublet in the spectrum of isolated mitochondria indicates that the bulk of the associated NHHS  $Fe^{II}$  species observed in our whole-cell spectrum was located in one or more non-mitochondrial regions of the cell (assumed for this study to be the cytosol). This is similar to the Fe content of Fe-deficient yeast cells. <sup>26</sup> In a previous study, <sup>28</sup> we showed that the relationship

$$[\mathit{Fe}]_{\mathit{cell}} - [\mathit{Fe}]_{\mathit{ferritin}} = [\mathit{Fe}]_{\mathit{mito}} \frac{V_{\mathit{mito}}}{V_{\mathit{cell}}} + [\mathit{Fe}]_{\mathit{other}} \left(1 - \frac{V_{\mathit{mito}}}{V_{\mathit{cell}}}\right)$$

followed from the conservation of matter. We also found that  $V_{mito}/V_{cell} \sim 0.2$  for Jurkat cells. Along with the concentrations obtained in the current study for 3FU cells, this relationship and ratio suggest that ca. 50  $\mu$ M of Fe in these cells (primarily the NHHS Fe<sup>II</sup> species) is found in regions other than mitochondria (e.g. the cytosol).

Equivalent samples of 3FU whole-cells and their isolated mitochondria were characterized by EPR (Figures S3 and S4) and UV-visible (Figure S5 and S6) spectroscopies. EPR signals were weak, consistent with the low concentration of EPR-active Fe in these cells. Spectra included signals in the high-field and g = 2 regions. Observed resonances at g = 6.3 and 5.4 were assigned to the mixed-valence state (Heme  $a_3$  Fe<sup>III</sup> Cu<sub>b</sub><sup>I</sup>) of the cytochrome c oxidase active-site. The g = 4.3 signal was assigned to HS Fe<sup>III</sup> species with rhombic symmetry. The g = 2 region included signals at g = 2.00, due to an unidentified organic radical, and at  $g_{ave} = 1.94$  and 1.90, due primarily to mitochondrial respiratory complexes. The standard set of Fe<sup>II</sup> heme UV-vis features were observed for all whole-cell and isolated mitochondria

samples. Our analysis suggests that the Fe content of these mitochondria are similar to that reported previously.<sup>28</sup>

#### Fe content of 30FU cells

30FU cells contained nearly 4-times more Fe than 3FU cells (Table 1) and 2-times more Fe than 10FU cells. <sup>28</sup> The corresponding 5 K low-field MB spectrum (Figure 3A) was dominated by a broad quadrupole doublet with parameters typical of Fe<sup>III</sup> oxyhydroxide nanoparticles ( $\delta$ = 0.48 mm/s,  $\Delta E_Q$  = 0.57). This doublet represented 65% of the Fe in the sample and corresponded to  $\sim$  550  $\mu$ M Fe (65% of 840  $\mu$ M total Fe). Nanoparticles were also present in 10FU cells but their concentration was 7-fold less.

The MB spectrum of 30FU cells also exhibited a ferritin-based sextet. Although barely distinguishable from baseline, the sextet represented ca. 13% of the Fe in the sample (0.13 × 840  $\mu$ M = 109  $\mu$ M). This concentration was almost the same as that of ferritin Fe in 3FU cells. Quantitative Western blotting (Figure 2) indicated  $\sim$  0.4  $\mu$ M ferritin protein in the sample, again suggesting partial Fe loading (109  $\mu$ M/0.4  $\mu$ M  $\approx$  300 Fe/ferritin). A similar analysis of 10FU cells also indicated partial ferritin loading (160  $\mu$ M/0.3  $\mu$ M  $\approx$  500 Fe/ferritin). The uncertainty in these determinations was such that loading ratios are considered to be essentially invariant for most all conditions, with an average of 400  $\pm$  100 Fe/ferritin (3 and 10  $\mu$ M TBI-grown cells have even lower loading ratios).

The Fe associated with ferritin and nanoparticles collectively accounted for all but 185  $\mu$ M Fe in the 30FU cells. Nanoparticles and ferritin-bound Fe probably do not contribute to cellular physiology; the majority of the remaining Fe is probably due to the essential Fe described above. The CD in the 5 K MB spectrum (Figure 3A) could not be cleanly resolved from the nanoparticles doublet; however, subtracting various percentages of a doublet fixed with CD parameters from the unresolved nanoparticle-dominated feature suggested that 10 - 15% of the spectral intensity (100 - 130  $\mu$ M) was due to the CD. At 70 K, the ferritin sextet collapsed into a doublet revealing a NHHS Fe<sup>II</sup> doublet (green line in Figure 3B) that corresponded to *ca.* 7% of spectral intensity (60  $\mu$ M Fe<sup>II</sup>). These two features, the CD and NHHS Fe<sup>II</sup>, undoubtedly represented much of the essential Fe in the sample. Somewhat lower concentrations of these two species were observed in the 3FU sample.

The extent of nanoparticle formation scaled nonlinearly with the concentration of Fe in the medium. 100FU cells were grown to maximize formation of these particles; such a sample was characterized by MB spectroscopy at 5 K and 0.05 T (Figure 3C). These cells accumulated 3.5 - 4 mM total Fe, > 90% of which was in the form of nanoparticles. The corresponding 6 T spectrum (Figure 3D, black hashmarks) was dominated by a broad magnetic feature suggesting superparamagnetic behavior. This spectrum was compared to that of previously-characterized Fe<sup>III</sup> oxyhydroxide phosphorous-associated nanoparticles from the Aft1-1<sup>up</sup> yeast strain<sup>27</sup> (Figure 3D, red line). Spectral features were similar but not identical, indicating a different distribution of hyperfine coupling constants. These magnetic differences must correspond, at some level, to structural differences.

MB spectra of mitochondria isolated from 30FU cells were also dominated by nanoparticles (Figure 3E, Table S1). Approximately 690  $\mu M$  Fe in these isolated organelles originated from nanoparticles whereas the concentration of nanoparticles in corresponding whole cells was  $\sim 550~\mu M$ . Since mitochondria occupy  $\sim 20\%$  of the cell's volume, we would expect that if all nanoparticles in the cell were present in these organelles, the concentration of nanoparticles in isolated mitochondria would be  $\sim 2.7~mM$  Fe (5× more than observed). Furthermore, upon increasing the FC concentration from 10 to 30  $\mu M$  in the medium, the whole-cell Fe concentration doubled, but the Fe concentration associated with isolated mitochondria did not change significantly. These considerations imply that the extra Fe in

30FU cells (primarily nanoparticles) accumulated in one or more non-mitochondrial regions, possibly in the cytosol.

Although the concentration of Fe in 30FU mitochondria was similar to that of 10FU mitochondria, <sup>28</sup> the MB distribution of that Fe was different. Mitochondria from the 30FU cells exhibited a significant decrease in absolute concentration of ferritin-like Fe, HS Fe<sup>II</sup> hemes, and NHHS Fe<sup>II</sup>, as well as a significant increase in nanoparticles (Table S2). The diminished amount of ferritin-like Fe may be irrelevant given that ferritin is cytosolic. The difference in ferritin-like material is probably the consequence of small-number-variations (we prepared two batches at each concentration) and less contamination in the 30FU samples. UV-vis analysis of these samples exhibited similar levels of cytochromes (Figure S6). EPR spectra were also determined for 3FU and 30FU cells. The same group of signals, with similar intensities, was observed as for a 10FU sample. <sup>28</sup> The spectral intensities of the CD component of MB spectra were similar for the samples. These characteristics, considered collectively, suggest that the concentrations of respiratory complexes in the mitochondria isolated from 3FU, 10FU, and 30FU cells were approximately the same. The major difference was the presence of more nanoparticles in the 30FU cells.

We were initially concerned that the doublet attributed to nanoparticles in these cells actually represented ferritin loaded with small amounts of Fe (  $\,$  10:1 Fe:Ferritin ratio). At  $\sim$  4 K, such species exhibit quadrupole doublets rather than a sextet.  $^{38}$  We reasoned that if the superparamagnetic doublet actually arose from poorly-loaded ferritin, adding an excess of Fe II under aerobic conditions would load the ferritin, causing the doublet to disappear and the sextet to appear. However, the results (Figure S2) did not show such a shift, indicating that the majority of the broad doublet arose from nanoparticles rather than from poorly-loaded ferritin.

EDX EM imaging of 30FU cells revealed  $\sim 1$  nm diameter particles in what appears to be the cytosol (Figure 4C). Elemental mapping revealed that these particles were associated with both Fe and P in approximately a 1:1 molar ratio (Figures 4A-B and S1). Results for O were ambiguous due to strong background levels of O in the cytosol and/or in the embedding medium. Such nanoparticles were not detected by EDX imaging in 3FU or 3TU cells.

#### **Oxidative Damage**

In yeast cells, nanoparticle formation is reportedly associated with oxidative damage.<sup>39, 40</sup> To investigate whether nanoparticle formation is associated with oxidative damage in human cells, we performed an Oxyblot analysis on 3FU 10FU, 30FU and 100FU Jurkat cells (Figure 5, lanes 1 - 4). In this experiment, the level of oxidative damage increased modestly as FC and nanoparticle levels increased. In another experiment (Figure S7), there was no correlation between ROS and Fe level. We conclude that there is little effect of nanoparticle formation on ROS levels in glucose-grown Jurkat cells.

#### Bioavailability of nanoparticles

We wondered whether cells can utilize the Fe in nanoparticles. Cells were overloaded with nanoparticles (by growth in  $20 \,\mu\text{M}^{57}\text{FC}$  medium) and then transferred to unsupplemented medium. They were grown to maximum density, and a portion was used to prepare a MB sample. Remaining cells were washed once with PBS containing 1 mM EGTA (to remove excess Fe), followed by another wash with PBS buffer lacking EGTA. The cells were diluted 4-fold in unsupplemented medium, allowed to grow to maximum density (two doubling times), and then harvested. 20FU cells accumulated significant amounts of nanoparticles (Figure 6A), but nanoparticles were absent in the cells that were subsequently

grown on unsupplemented medium; only the CD, ferritin, NHHS Fe<sup>II</sup> and HS Fe<sup>II</sup> hemes were evident in the 5 K low-field MB spectrum (Figure 6B). Metal analysis combined with MB simulations of different Fe species (Table 1) indicated that the only feature that declined considerably in concentration (> 40-fold decrease) upon growth of the split cells was nanoparticles. Other features remain roughly unchanged, with minor decreases attributed mainly to dilution due to growth of the cells. These results indicate that Jurkat cells can utilize nanoparticle Fe, converting it into mitochondrial Fe, ferritin, and presumably all other Fe-containing species required for cellular metabolism.

#### Galactose-grown cells

Cells were grown with 3, 10, and 30  $\mu$ M  $^{57}FC$  in medium containing galactose rather than glucose as a carbon source. 3FL cells accumulated  $\it ca.$  half as much Fe as 3FU cells. However, the Fe concentration of galactose-grown cells increased faster than did glucose-grown cells as the FC concentration in the growth medium was raised. The concentration of Fe in 10FL cells was  $\sim$  50% higher than in corresponding glucose-grown cells. 30FL cells contained > twice as much Fe as the corresponding glucose-grown cells (Table 1). Galactose-grown cells had a longer doubling time ( $\it ca.$  34 hr) which may have promoted Fe uptake.

MB analysis revealed that 3FL cells were largely devoid of nanoparticles (Figure 7A, Table 1). Interestingly, the 5 K 0.05 T MB spectrum of 10FL cells exhibited a 3-fold *greater* contribution from nanoparticles and a decline of ferritin Fe relative to 10FU cells (Figure 7B and Table 1). The nanoparticle doublet obscured the CD in the MB spectrum of galactosegrown cells, but simulation of the MB spectrum afforded an estimate of the percentage due to the CD. The low-intensity NHHS Fe<sup>II</sup> doublet was evident, with a concentration similar to that observed for 10FU cells. The absolute concentrations of nanoparticles (and possibly the CD) were significantly larger in 30FL cells than in equivalent glucose-grown cells (Figure 7C, Table 1). Distinguishing these two contributions is difficult because they are not well resolved. UV-vis spectra of galactose-grown cells do not exhibit increased concentrations of cytochromes (Figure S5) suggesting that there is no significant increase in mitochondria concentration (and thus no significant increase in the CD). The concentration of ferritin Fe also did not change considerably in galactose-grown cells upon increasing the FC concentration in the medium.

The observed difference in nanoparticle level might be related to the different metabolic activity of galactose- vs. glucose-grown cells, and/or to different growth rates. The oxygen consumption (OCR) rate of galactose-grown cells was 2 - 3 times greater than that of glucose-grown cells (Figure 8A). On the other hand, the extra-cellular acidification rate (ECAR) of the glucose-grown cells was 3 - 4 times greater than that of the galactose-grown cells. The OCR of cells grown under the two different carbon sources was also determined in the absence and presence of oligomycin (an inhibitor of  $F_1F_0$  ATP synthase). The normalized OCR of glucose-grown cells decreased  $\sim$ 60% in the presence of oligomycin, whereas that of galactose-grown cells decreased almost  $\sim$ 80% (Figure 8B) indicating tight coupling of respiration and ATP synthesis in galactose-grown cells. These results confirm that our galactose-grown cells depended more heavily on oxidative phosphorylation (i.e. mitochondrial respiration) for ATP production than they did on glycolysis.

#### **Oxidative Damage**

Cells grown on galactose and FC exhibited  $\sim 50\%$  higher levels of oxidative damage than cells grown on glucose and FC (Figure 5). The effect of cellular Fe concentration on the level of ROS damage was again minor, if any. The increased damage to galactose grown

cells may be caused by the greater dependency on mitochondrial respiration and oxidative phosphorylation for ATP production in galactose-grown cells.<sup>41</sup>

# Increased transferrin-receptor expression

Cells were grown on medium supplemented with 3TU. The total Fe concentration in such cells was quite low ( $\it{ca}$ . 140  $\mu$ M) and the  $^{57}$ Fe enrichment was only  $\sim$  50%. Consequently, the corresponding 5 K low-field MB spectrum (Figure 9A) had a low percent-effect and was noisy. The general pattern indicated less ferritin and relatively more CD, compared to the Fe content of 3FU cells. Spectral noise precluded a more detailed analysis. MB spectra of mitochondria isolated from cells grown with 3TU (Figure 9C) exhibited little evidence of a nanoparticle doublet.

Increasing the  $^{57}TBI$  concentration in the medium to 30  $\mu M$  yielded an intracellular Fe concentration of 225  $\mu M$ , which resulted in a more intense and analyzable 5 K low-field MB spectrum (Figure 9B). The spectrum was dominated by ferritin and CD Fe, and displayed a negligible nanoparticle doublet (Table 1). The extent of ferritin loading was  $\sim\!3$  times larger than in 3TU or 10TU cells (Table 1), but was still low ( $\sim300$  Fe/ferritin) relative to full loading.

In an effort to increase the Fe concentration in TBI-grown cells, cells were genetically modified to overexpress  $\sim\!\!3$ -fold more TfRC1 than normal (Figure S8). Such cells (called TfRC+) grown on 3  $\mu$ M  $^{57}$ TBI contained 3-times as much total Fe as equivalently grown WT cells. Correspondingly, the MB spectrum exhibited by the TfRC1+ cells (Figure 9D) was more intense. Sixty percent of the Fe in the cells was ferritin-bound, which was the highest percentage of Fe found in this form for any cell conditions examined. The sextet contribution was simulated and removed, revealing CD and NHHS Fe^{II} contributions. The spectrum included little if any nanoparticle doublet. TfRC+ cells were also grown with 10  $\mu$ M  $^{57}$ TBI; such cells accumulated  $\sim$  25% more Fe than cells grown with 3  $\mu$ M  $^{57}$ TBI. MB analysis of these cells revealed a more significant accumulation of nanoparticles (Figure 9E and Table 1).

We also attempted to stimulate WT cells to uptake TBI by first starving them of Fe in the presence of DFO for 12 hours (to upregulate TfRC1 expression), and then adding 3  $\mu$ M <sup>57</sup>TBI to the growth culture. These cells incorporated *ca.* 3 times more <sup>57</sup>Fe than cells grown on 3  $\mu$ M <sup>57</sup>TBI without this stimulation. They accumulated Fe mainly in the form of ferritin and CD (Figure 9F, Table 1).

#### **Reduced Frataxin Expression**

We also examined the Fe content of Jurkat cells in which frataxin expression was reduced by RNAi. Western blot analysis indicated that the expression level of frataxin in frataxin-deficient cells was 30-50% that of WT levels in cells grown under the same conditions (10  $\mu$ M FC) (Figure S9). Frataxin-deficient cells grown with 10  $\mu$ M FC accumulated significantly more nanoparticles than 10FU cells (Figure 10; Table 1). The concentration of nanoparticles detected by MB spectroscopy was  $\it ca.$  3× greater in frataxin-deficient cells (220  $\mu$ M  $\it vs.$  72  $\mu$ M in WT cells). These cells accumulated more total cellular Fe than WT cells (550  $\mu$ M  $\it vs.$  400  $\mu$ M), with most of the excess Fe present as nanoparticles. UV-Vis analysis indicated a  $\sim$  40% decline in cytochrome levels of frataxin-deficient cells relative to WT cells (Figure S10).

# **Analysis**

We analyzed our data by developing a chemical model for the Fe import and trafficking pathways in Jurkat cells (Figure 11). Cellular Fe was assumed to be composed of 4 species,

namely  $[Fe_{cell}] = [Fe_c] + [Fe_f] + [Fe_m] + [Fe_n]$ . Fe could enter the cell by either TBI or FC import pathways. Both pathways merged at Fe<sub>c</sub>, an unidentified cytosolic Fe species presumed to correspond to the NHHS Fe<sup>II</sup> spectral feature observed in MB spectra of Jurkat cells. According to the model, Fe<sub>c</sub> can react to form Fe<sub>f</sub>, Fe<sub>m</sub> and Fe<sub>n</sub>, which represent the Fe associated with ferritin, mitochondria and nanoparticles, respectively. Fe<sub>m</sub> is the sum of cellular Fe-S clusters and hemes, which we assumed to be originating exclusively from mitochondria.

The model of Figure 11 was translated into ordinary differential equations (ODE's) [1] -[4] which describe the factors that influence the changes in concentration of each cellular component.

$$\frac{d[Fe_c]}{dt} = \frac{k_t[TBI]}{1 + \left(\frac{[Fe_c]}{K_{Ic}}\right)^{cs}} + k_r[FC] - \frac{k_m[Fe_c]}{1 + \left(\frac{[Fe_m]}{K_{Im}}\right)^{ms}} - \frac{k_f[Fe_c]}{1 + \left(\frac{[Fe_f]}{K_{If}}\right)^{fs}} - k_n[Fe_c]^p - \alpha[Fe_c]$$
[1]

$$\frac{d[Fe_f]}{dt} = \frac{k_f[Fe_c]}{1 + \left(\frac{[Fe_f]}{K_{If}}\right)^{fs}} - \alpha[Fe_f] \quad [2]$$

$$\frac{d[Fe_m]}{dt} = \frac{k_m[Fe_c]}{1 + \left(\frac{[Fe_m]}{K_{\text{Im}}}\right)^{ms}} - \alpha[Fe_m] \quad [3]$$

$$\frac{d[Fe_n]}{dt} = k_n [Fe_c]^p - \alpha [Fe_n] \quad [4]$$

The first term on the right-hand-side of equation [1] describes the rate of import of TBI through the TfRC1 on the plasma membrane. Regulation of this and two others rates in the model are described by the function

$$\operatorname{Reg}_{-}(Fe_{s}, K_{I_{s}}, s) = \frac{1}{1 + \left(\frac{[Fe_{s}]}{K_{I_{s}}}\right)^{s}}$$

in which species  $Fe_s$  is sensed by the regulatory system,  $K_{Is}$  is an apparent inhibition constant associated with the sensing event (also called a set-point concentration), and s is a sensitivity parameter.  $Reg_{\_}$  is a form of the Hill equation that we have used as a surrogate for poorly defined or highly complex regulatory mechanisms.  $Reg_{\_}$  could reflect the direct (or indirect) binding of  $Fe_s$  to: a) the promoter of a gene (i.e. transcriptional regulation); b) an mRNA strand (translational regulation); or c) an allosteric site of a protein (enzyme regulation).  $Reg_{\_}$  can be viewed as a valve that opens wide when  $[Fe_s] < K_{Is}$ , shuts down when  $[Fe_s] > K_{Is}$ , and is half-opened when  $[Fe_s] = K_{Is}$ . The rate of TBI influx is regulated by  $Reg_{\_}$ , with  $Fe_c$  serving as  $Fe_s$ . In this case,  $Reg_{\_}$  is a surrogate for the Fe-dependent binding of IRP1/2 to the mRNA of the transferrin receptor mRNA.

The second term of [1] reflects the *unregulated* import of FC. Our model is minimal in that no unnecessary terms are included. We could fit the data in Table 1 acceptably well without assuming that the import of FC was regulated. The third term of [1] reflects the flow of Fe<sub>c</sub>

into mitochondria. The rate of mitochondrial Fe import via mitoferrin 1/2 is regulated but the mechanism has not been established in non-erythroid cells, except for the fact that these proteins are regulated post-translationally.  $^{42, 43}$  The sensed molecule in this process was assumed to be the concentration of mitochondrial Fe<sub>m</sub>.

The fourth term of [1] reflects the loading of Fe into ferritin. IRP1/2 also regulate ferritin synthesis in an Fe-dependent manner, stimulating production of ferritin under high-Fe conditions. We initially tried to regulate the system in this manner (by multiplying the rate of Fe loading into ferritin ( $k_f$ ) by the function  $Reg_+ = 1 - Reg_-$ , using Fe<sub>c</sub> as the sensed molecule) but the resulting behavior was not satisfactory, as the observed ferritin concentrations changed significantly less than the simulated concentrations. This suggested that the regulation of ferritin loading was more like the regulation of mitochondrial Fe import. Thus, we employed the  $Reg_-$  function in the manner used to regulate mitochondrial Fe import, assuming that the sensed Fe<sub>s</sub> was ferritin Fe<sub>f</sub>.

The fifth term of [1] refers to the rate of nanoparticle formation. We initially assumed a first-order dependence of [Fe\_c] in this process, but our simulations could not reproduce the disproportionate increase in nanoparticles (Fe\_n) that occurred when the FC concentration in the growth medium increased (e.g. from 3  $\rightarrow$  30 or  $\rightarrow$ 100  $\mu M$ ). Mimicking this behavior required that we assumed a higher-order dependence on [Fe\_c] (Table 1). This order-dependence is consistent with a mechanism in which multiple ( $\sim$  3) Fe ions react at or before the rate-determining step in the formation of nanoparticles.

The last term of [1] reflects dilution due to cell growth. In our model, the cell is growing as Fe is imported, such that a steady-state  $Fe_{cell}$  concentration is eventually achieved (the Fe concentration data of Table 1 was interpreted as representing steady-state values). Each component of a growing cell requires a dilution term in its ODE.<sup>44</sup> The growth rate  $\alpha$  was assumed to be the inverse of the doubling time.

The sum of ODEs [1] - [4]

$$\frac{d[Fe_{cell}]}{dt} = \frac{k_t[TBI]}{1 + \left(\frac{[Fe_c]}{K_{Ic}}\right)^{cs}} + k_r[FC] - \alpha[Fe_{cell}]$$

defines how the overall Fe concentration of the cell changes in time. In the absence of TBI and under Fe-limiting steady-state growth conditions,  $k_r[FC] = a[Fe_{cell}]$ . [FC] in this equation includes not only the concentration of ferric citrate in the medium, but the endogenous Fe (4 - 6  $\mu$ M). In the absence of additional added FC, [Fe<sub>cell</sub>]  $\approx 100 \,\mu$ M and [FC] = 4  $\mu$ M such that a DT of 24 hr implies that  $k_r \approx 0.7 \, hr^{-1}$ . When grown on 100  $\mu$ M FC, [Fe<sub>cell</sub>] = 3500  $\mu$ M, [FC] = 106  $\mu$ M, and thus  $k_r \approx 1.3 \, hr^{-1}$ . We view this range for  $k_r$  (1.0  $\pm$  0.3) as acceptable, given the simplicity of the model.

Sensitivity factors ms and fs were set semi-arbitrarily to 10 to provide extremely tight regulation. The other parameters of the system  $(cs, K_{Ic}, K_{Im}, K_{If}, k_t, k_m, k_f, k_n \text{ and } p)$  were estimated by attempting to simulate the entire dataset of Table 1. The ODEs were numerically integrated using Maple software (http://www.maplesoft.com/). Growth conditions of the simulation model cell were varied to mimic the conditions listed in Table 1. For TfRC+ cells, the constitutive overexpression of TfRC was mimicked by assuming a 6-fold faster import rate constant  $k_t$  AND by removing the  $Reg_-$  term. Cells grew slower on galactose than on glucose (DT = 34 hr rather than 24 hr) so  $\alpha$  was adjusted accordingly for those simulations. Each simulation was allowed to continue for 1000 hr (where time refers

to that indicated in the ODEs) to assure that steady-state conditions had been achieved. Resulting simulated concentrations are given in Table 1. The uncertainties associated with the data were estimated to be  $\pm$  20% so that discrepancies between simulations and data within this range are considered irrelevant. The model is simple, semi-quantitative, and foundational. It captures the essential features of Fe import and trafficking in Jurkat cells, but lacks many details associated with these processes.

One advantage of ODE models is that they have predictive power. Thus, our model can predict the distribution of these 4 forms of Fe in Jurkat cells grown with any concentration of TBI or FC. It can also be modified so as to explore genetic changes in the cell - such as the consequences of reducing the expression level of frataxin. Previous studies in yeast and mice have shown that a frataxin deficiency causes the accumulation of nanoparticles in mitochondria. This leads to an Fe-deficiency condition in the cytosol.  $^{30,45,46}$  To examine how our model would respond to this phenotype, we allowed for the possible formation of nanoparticles in the mitochondria (by adding the term  $(-k_{np} [Fe_m]^p)$  to the ODE of equation [3] and by adding ODE [5]

$$\frac{d[Fe_{mp}]}{dt} = k_{mp}[Fe_m]^{mp} - \alpha[Fe_{mp}] \quad [5]$$

to the set of ODEs [1] – [4]. For simplicity, we assumed that the kinetics of nanoparticle formation in the mitochondria were the same as for nanoparticle formation in the original model (presumably in the cytosol). As such, we assigned  $k_{mp}$  and mp to the same values assigned to  $k_{np}$  and p, respectively.

As a control, we solved the new system assuming  $k_{mp} = 0$  and  $\alpha = 1/24 \text{ hr}^{-1}$  so as to mimic WT expression levels of frataxin and the growth rate of WT cells. Resulting steady-state simulated concentrations are shown in the early region of the plot of Figure 12. We then set  $k_{mp} = 0.00045 \text{ hr}^{-1}$  and  $\alpha$  to  $1/30 \text{ hr}^{-1}$  to stimulate mitochondrial nanoparticle formation and mimic the slower-growing frataxin-deficient cells. The overall Fe concentration increased in our simulations from 461 to 528  $\mu$ M, similar to the final state observed experimentally. The predicted time-dependences of these changes should be evaluated experimentally, but this is beyond the scope of the current study. The simulated response included an increase in mitochondrial nanoparticles as well as a decline of non-nanoparticle forms of mitochondrial Fe (interpreted as Fe/S clusters, hemes and the pool of NHHS Fe<sup>II</sup>). These changes are consistent with the deficiencies of Fe/S clusters and hemes that are associated (along with the dominance of nanoparticles) with the frataxin phenotype. <sup>47</sup> The simulated response to frataxin deficiency also included a decline of cytosolic and ferritin Fe, consistent with the cytosolic Fe-deficiency phenotype that has been reported. <sup>46</sup> We repeated the simulation at 3  $\mu$ M FC concentration, but no phenotype was evident.

#### **Discussion**

Using MB spectroscopy and other biophysical methods, we have investigated the Fe import pathways and downstream trafficking of two forms of Fe in human Jurkat cells, namely transferrin-bound iron (TBI) and ferric citrate (FC). We did this by characterizing the Fe content of such cells grown in media containing different concentrations of TBI and/or FC and different carbon sources (glucose *vs.* galactose). We also investigated cells in which the expression levels of the transferrin-receptor and frataxin were altered. We developed a mathematical model of Fe import and trafficking in these cells, and fitted simulations obtained therefrom to our data.

#### **TBI and FC Import Pathways**

Our data and simulations indicate that the *import of TBI iron is highly regulated*. Our model suggests that cytosolic Fe regulates TBI import in accordance with a set-point concentration of ca. 9  $\mu$ M. In contrast, the *import of FC does not appear to be regulated*, or at least our model did not require that assumption. Whether the same holds true of other forms of NTBI remains to be determined, but we regard this as a viable possibility.

The fate of TBI (after DMT1-promoted export from endosomes into the cytosol) and the fate of FC within the cell are largely unknown. An earlier version of the model assumed two forms of cytosolic Fe, one derived from TBI and the other from FC. However, this assumption did not improve the fits and so we merged the two import pathways immediately once Fe entered the cytosol. In real cells, the pathways may not merge immediately. However, they must eventually merge. Fe from either source eventually traffics into mitochondria (via the IM transporters mitoferrin1/2<sup>48</sup>), loads into ferritin (via PCBP1/2 chaperones<sup>49,50</sup>), and forms nanoparticles. There is probably no dedicated protein chaperones that traffics Fe into nanoparticles. Rather, these particles appear to form spontaneously via chemistry of which the cell is unaware.

The distribution of Fe in TBI-grown cells differs relative to that in cells grown on the same concentration of FC, primarily because less Fe overall is imported into TBI-grown cells. This is due, in turn, to the tighter regulation of TBI import. The higher concentration of cytosolic Fe in FC-grown cells increases the rate of nanoparticles formation disproportionately, such that it dominates the Fe content of FC-grown cells but not TBI-grown cells. Consistent with this, TBI-grown cells in which the transferrin-receptor was constitutively overexpressed contained higher concentrations of Fe, relative to WT cells grown on TBI. The distribution of Fe in these cells was similar but not identical to that observed in FC-grown cells.

Another likely reason for the different Fe distributions is that the TBI pathway may somehow favor storing Fe as ferritin relative to the FC pathway which tends to funnel more Fe into nanoparticles. Our current model does not include such distinctions, but the possibility of distinct intracellular pathways should be considered when developing more advanced models. Supporting such a distinction at the protein expression level, our data show a more sensitive upregulation of ferritin protein in TBI-grown cells relative to in FC-grown cells. For example, 3TU cells had twice the concentration of ferritin compared to 3FU cells. This suggests that the IRP1/2 system of regulation responds more sensitively to Fec derived from TBI. Furthermore, TfRC+ cells grown on 3  $\mu$ M TBI accumulated the same cellular Fe concentration as 10FU WT cells, but that Fe included significantly fewer nanoparticles and more ferritin Fe. Our simple model cannot account for such differences.

#### Mitochondria

The concentrations of mitochondrial Fe centers, including Fe-S clusters, hemes and HS Fe<sup>III</sup> ions, do not change drastically upon increasing the medium Fe concentration. This indicates the ability of mitochondria to regulate their own Fe import. The expression of the only known Fe transporters in the mitochondrial membrane, mitoferrin 1 and mitoferrin 2 (Mfrn1 and Mfrn2) is tightly regulated to prevent excessive mitochondrial Fe accumulation. <sup>43</sup> To mimic this invariance, our model tightly regulated mitochondrial Fe import using mitochondrial Fe itself as the sensed species. Clearly, not all mitochondrial Fe is sensed. Nevertheless, this regulatory assumption would remain viable as long as the concentration of the sensed molecule was proportional to the overall mitochondrial Fe concentration. The concentration of nanoparticles in mitochondria does seem to increase with the concentration

of Fe in the medium. Again, this form of Fe may not be regulated by the cell; indeed the cell may be unaware of its existence.

#### **Ferritin**

The extent of Fe loading into ferritin was an order-of-magnitude less than the often-quoted value of 4500 Fe per core. Moreover, the extent of loading did not increase with increasing Fe concentration in the growth medium (which we presume is proportional to the cytosolic Fe concentration). Both results were surprising.

The low average extent of loading is undoubtedly due to a distribution of loading levels in a population of ferritin molecules. Ferritin-loading distributions have been previously described for ferritin purified from various organs, using ultracentrifugation or MB spectroscopy coupled with electron microscopy. Bovell *et al.* obtained similar results by performing *in situ* electron microscopy coupled with ASAX analysis on rat liver sections. We suggest a binomial distribution of Fe loadings in ferritin populations of Jurkat cells, with a maximum approaching 4500 Fe per ferritin and a mean near  $\sim$  400 Fe/ferritin. Our studies also suggest that the average ferritin load remains about the same regardless of the overall Fe concentration in the cell (though perhaps lower load in 3TU and 10TU cells). Our results are consistent with an EM study showing a distribution of ferritin loading in iron-overloaded rat livers.

The popular explanation of IRP1/2 regulation of ferritin is that the unbinding of these proteins to the ferritin message under high cytosolic Fe concentrations promotes ferritin synthesis *so that* excess cytosolic Fe can be removed from the cytosol and stored in ferritin.<sup>6</sup> The implication is that without this promotion, there would be no way for excess cytosolic Fe to be removed - *because the existing ferritin was already fully loaded*. The regulation of ferritin and the extent of loading do not appear to be so simple, at least in Jurkat cells. Cells containing partially loaded ferritin responded to increasing (cytosolic/medium) Fe concentrations by synthesizing more ferritin proteins, not by loading pre-existing ferritin to the fullest possible extent. Another spurious initial notion of ours was that nanoparticles would form only once the cell exhausted its ferritin-binding capacity. In contrast, we found that the ferritin was partially loaded in FC-grown cells that also contained substantial quantities of nanoparticles.

One explanation of this partial-loading behavior is that the set-point concentrations for ferritin synthesis and Fe-loading of ferritin differ. The set-point concentration of the Fe species that regulates the synthesis of new ferritin protein (via the IRP1/2 system) might be lower than the concentration of Fe required to fully load ferritin. In this way, as cytosolic Fe levels increase, they trigger further ferritin protein synthesis such that existing ferritin never becomes fully loaded.

Another shift in our thinking arose from our attempt to model the concentration of ferritin Fe in cells grown under different conditions. The concentration of ferritin Fe was roughly invariant among all of the conditions tested and examined by MB spectroscopy (Fe-limited cells and Fe-overloaded cells could not be investigated by MB). We initially attempted to model this using the well-known IRP1/2 mechanism. This required a  $Reg_+$  function in which Fe<sub>c</sub> was sensed. However, this resulted in *greater* variation in Fe ferritin levels than was evident in the data. Thus, we abandoned that form of regulation and employed a  $Reg_-$  function in which ferritin Fe<sub>f</sub> was sensed (we did this after noting how well mitochondrial Fe could be regulated by assuming the  $Reg_-$  function with Fe<sub>m</sub> as the sensed molecule). This arrangement adequately reproduced ferritin Fe levels under the various circumstances examined. However, the molecular-level mechanism responsible for this form of regulation is not understood; it seems unlikely that ferritin Fe could directly be sensed since it is an

aggregated form. The rate of Fe import into ferritin might be inhibited as the degree of ferritin loading reaches some critical threshold, as has been suggested based on the rates of ferritin loading *in vitro*. <sup>53, 54</sup>

#### **Nanoparticles**

The nanoparticles that accumulate in Jurkat cells are similar in chemical composition to those found in strains of yeast that have mutations in Fe/S cluster metabolism proteins.  $^{39,\,40}$  The differences in high-field MB spectra, relative to yeast nanoparticles, suggest modest structural differences. Previous MB studies of the spleens of  $\beta$ -thalassemia patients indicate accumulation of a species with MB parameters similar to the nanoparticle doublet observed here. Ferric phosphate nanoparticles accumulate in the hearts of mice displaying symptoms of Friedreich's ataxia. The size of the particles observed in our cells are substantially smaller than ferritin particles ( $\sim 1$  nm vs. 2.8 - 8 nm) $^{36,\,56}$  and they contain more phosphorus than ferritins. Our results suggest that the majority of nanoparticles formed in these cells are non-mitochondrial. Our EM results suggest that nanoparticles form in the cytosol, and this was assumed by our model.

Our model suggests that the rate of nanoparticles formation is *not* regulated. This is consistent with the idea that the cell is unaware that nanoparticles are forming, suggesting that this is a purely chemical phenomenon. Although nanoparticles cannot be sensed by the cell, they may nevertheless play a role in cellular metabolism. We found that nanoparticles formation is reversible and that nanoparticle Fe can be recycled by the cell.

Our model required that the rate of nanoparticle formation depend on the cytosolic Fe concentration to higher than first order. This high-order rate dependence leads to the observed "burst" phenomenon in which there is a disproportionate increase in nanoparticles as the  $\rm Fe_c$  concentration increases. It implies that more than one  $\rm Fe^{III}$  ions (nominally 3 such ions, according to our simulations) come together to form nanoparticles at or before the rate-determining step in the process.

#### **Oxidative Damage**

The lack of correlation between the extent of nanoparticle formation and oxidative damage in FC-grown cells grown on glucose is consistent with the results of Hartwig *et al.* who found that oxidative damage to DNA and lipid peroxidation in glucose-grown mammalian cells is *not* induced by growth on up to 2 mM FC.<sup>58, 59</sup> Fe<sup>III</sup> nanoparticles form from the oxidation of Fe<sup>II</sup> ions, but whether this generates ROS (or is promoted by ROS) is uncertain. Our results indicate that the overall level of cellular ROS damage does NOT correlate significantly with cellular Fe or nanoparticle levels. Nanoparticle formation may generate (or be generated by) small amounts of ROS, but this doesn't impact cellular ROS levels significantly.

ROS can be scavenged by catalases, peroxidases and antioxidants.<sup>60, 61</sup> Perhaps the observed extent of oxidative damage is inversely related to the rate of these repairs. Also, metabolic mode and growth rate may be factors in the level of cellular ROS damage. These considerations are supported by our finding that galactose-grown cells (which are more active in terms of respiration and also grow more slowly) are associated with greater ROS damage.

Our results and conclusions regarding the insignificance of nanoparticle formation on overall cellular oxidative damage are literally *opposite* of that proposed by Whitnall *et al.*<sup>29</sup> who identified nanoparticles in the hearts of frataxin-deficient mice. They proposed that

nanoparticles may be an "explosive" (their emphasis) source of ROS in such diseased heart tissue. Our data suggest that nanoparticle formation has little impact on cellular ROS levels.

#### **Frataxin**

Although simple, our model reproduces the major effects of depleting cells of frataxin. Besides accumulating nanoparticles in the mitochondria (which was designed into the model), other cellular Fe species in the model responded in ways that are also observed experimentally. Frataxin-deficient cells "feel" Fe-deficient in the cytosol, due to the increased rate of Fe import into mitochondria. This effect was recreated in our simulations. Importantly, there was no alteration of the regulation of the entire system – including the regulation of Fe import into the mitochondria themselves. The increase in total mitochondrial Fe (including  $[Fe_m] + [Fe_{mp}]$ ) was associated with the *decline* in  $[Fe_m]$  as this form of Fe was used to make mitochondrial nanoparticles. This decline stimulated further Fe import into the organelle, which created a deficiency of Fe in the cytosol. Importantly, this imbalance of Fe in the cell was due to nanoparticle formation in the mitochondria, not to malfunctioning regulatory systems. Our study and model suggest that there is nothing "wrong" with Fe regulation in cells that are deficient in frataxin (or by extension, in patients with Friedrich's ataxia). The problem is that a deficiency of frataxin somehow alters the mitochondrial matrix so as to favor nanoparticle formation. This might involve changes in pH, redox state, or chemical composition. Understanding the mechanistic basis of these alterations will be critical in understanding and treating the disease.

## **Mathematical Modeling**

Interpreting changes in cellular Fe metabolism (or any other complex cellular metabolic subsystem) on the molecular/mechanistic level is difficult, as the complexity of these systems is enormous. As more molecular-level interactions are discovered and characterized, it becomes increasingly difficult (and will eventually become impossible) to draw mechanistic inferences based merely on mentally contemplating such interactions. Gaining mechanistic insights will increasingly require the aid of mathematical models that can include an unlimited number of relationships explicitly and can integrate their collective effects.

## Supplementary Material

Refer to Web version on PubMed Central for supplementary material.

# **Acknowledgments**

We thank Ann Ellis and Hansoo Kim at the Microscopy and Imaging Center at Texas A&M University for help in collecting images.

**Funding Statement:** This study was funded by the National Institutes of Health (GM084266), the Robert A. Welch Foundation (A1170) and the National Science Foundation (DMS-0714896).

# References

- 1. Anderson GJ, Vulpe CD. Mammalian iron transport. Cell Mol Life Sci. 2009; 66:3241–3261. [PubMed: 19484405]
- 2. Hentze MW, Muckenthaler MU, Galy B, Camaschella C. Two to Tango: Regulation of Mammalian Iron Metabolism. Cell. 2010; 142:24–38. [PubMed: 20603012]
- 3. Garrick MD, Garrick LM. Cellular iron transport. Bba-Gen Subjects. 2009; 1790:309–325.
- 4. Huebers H, Josephson B, Huebers E, Csiba E, Finch C. Uptake and release of iron from human transferrin. Proc Natl Acad Sci. 1981; 78:2572–2576. [PubMed: 6941310]

 Tabuchi M, Kishi F. Human NRAMP2/DMT1, Which Mediates Iron Transport across Endosomal Membranes, Is Localized to Late Endosomes and Lysosomes in HEp-2 Cells. J Biol Chem. 2000; 275:22220–22228. [PubMed: 10751401]

- Muckenthaler MU, Galy B, Hentze MW. Systemic Iron Homeostasis and the Iron-Responsive Element/Iron-Regulatory Protein (IRE/IRP) Regulatory Network. Annu Rev Nutr. 2008; 28:197–213. [PubMed: 18489257]
- 7. Theil EC. Ferritin: Structure, Gene Regulation, and Cellular Function in Animals, Plants and Microorganisms. Ann Rev Biochem. 1987; 56:289–315. [PubMed: 3304136]
- 8. Brissot P, Ropert M, Le Lan C, Loreal O. Non-transferrin bound iron: A key role in iron overload and iron toxicity. Biochim Biophys Acta. 2012; 1820:403–410. [PubMed: 21855608]
- Evans RW, Rafique R, Zarea A, Rapisarda C, Cammack R, Evans PJ, Porter JB, Hider RC. Nature of non-transferrin-bound iron: studies on iron citrate complexes and thalassemic sera. J Biol Inorg Chem. 2008; 13:57–74. [PubMed: 17906879]
- 10. Hider RC. Nature of nontransferrin-bound iron. Eur J Clin Inv. 2002; 32:50-54.
- 11. Jordan I, Kaplan J. The mammalian transferrin-independent iron transport system may involve a surface ferrireductase activity. Biochem J. 1994; 302:875–879. [PubMed: 7945215]
- Picard V, Govoni G, Jabado N, Gros P. Nramp2 (DCT1/DMT1) Expressed at the Plasma Membrane Transports Iron and Other Divalent Cations into a Calcein-accessible Cytoplasmic Pool. J Biol Chem. 2000; 275:35738–35745. [PubMed: 10942769]
- 13. Liuzzi JP, Cousins RJ. Zip14 (Slc39a14) mediates non-transferrin-bound iron uptake into cells. Proc Natl Acad Sci. 2006; 103:13612–13617. [PubMed: 16950869]
- 14. Oudit GY, Backx PH. L-type Ca2+ channels provide a major pathway for iron entry into cardiomyocytes in iron-overload cardiomyopathy. Nat Med. 2003; 9:1187–1194. [PubMed: 12937413]
- Sohn YS, Ghoti H, Breuer W, Rachmilewitz EA, Attar S, Weiss G, Cabantchik ZI. The role of endocytic pathways in cellular uptake of plasma non-transferrin iron. Haematologica. 2011; 97:670–678. [PubMed: 22180428]
- Breuer W, Ghoti H, Shattat A, Goldfarb A, Koren A, Levin C, Rachmilewitz E, Cabantchik ZI. Non-transferrin bound iron in Thalassemia: differential detection of redox active forms in children and older patients. Am J Hematol. 2012; 87:55–61. [PubMed: 22125177]
- Grootveld M, Bells JD, Halliwell B, Aruoma OI, Bomford A, Sadler PJ. Non-transferrin-bound Iron in Plasma or Serum from Patients with Idiopathic Hemochromatosis. J Biol Chem. 1989; 264:4417–4422. [PubMed: 2466835]
- 18. Bernstein SE. Hereditary hypotransferrinemia with hemosiderosis, a murine disorder resembling human atransferrinemia. J Lab Clin Med. 1987; 110:690–705. [PubMed: 3681112]
- 19. Valk BD, Marx JJM. Non-transferrin-bound iron is present in serum of hereditary haemochromatosis heterozygotes. Eur J Clin Inv. 2000; 30:248–251.
- 20. SanMartín C, Paula-Lima A, Hidalgo C, Núñez M. Sub-lethal levels of amyloid β-peptide oligomers decrease non-transferrin-bound iron uptake and do not potentiate iron toxicity in primary hippocampal neurons. BioMetals. 2012:1–9.
- Baker E, Baker SM, Morgan EH. Characterisation of non-transferrin-bound iron (ferric citrate) uptake by rat hepatocytes in culture. Biochim Biophys Acta. 1998; 1380:21–30. [PubMed: 9545519]
- Brissot P, Wright TL, Ma WL, Weisiger RA. Efficient Clearance of Non-transferrin-bound Iron by Rat Liver. J Clin Invest. 1985; 76:1463–1470. [PubMed: 4056038]
- Sturrock A, Alexander J, Lamb J, Craven CM, Kaplan J. Characterization of a Transferrinindependent Uptake System for Iron in HeLa cells. J Biol Chem. 1990; 265:3139–3145. [PubMed: 2105943]
- 24. Kaplan J, Jordan I, Sturrock A. Regulation of the Transferrin-independent Iron Transport System in Cultured Cells. J Biol Chem. 1991; 266:2997–3004. [PubMed: 1993673]
- 25. Inman RS, Wessling-Resnick M. Characterization of Transferrin-independent Iron Transport in K562 Cells. J Biol Chem. 1993; 268:8521–8528. [PubMed: 8473296]

 Holmes-Hampton G, Jhurry ND, McCormick SP, Lindahl PA. Iron Content of Saccharomyces cerevisiae Cells Grown under Iron-Deficient and Iron-Overload Conditions. Biochemistry. 2013; 52:105–114. [PubMed: 23253189]

- Miao R, Holmes-Hampton G, Lindahl PA. Biophysical Investigation of the Iron in Aft1-1up and Gal-YAH1 Saccharomyces cerevisiae. Biochemistry. 2011; 50:2660–2671. [PubMed: 21361388]
- Jhurry ND, Chakrabarti M, McCormick SP, Holmes-Hampton G, Lindahl PA. Biophysical Investigation of the Ironome of Human Jurkat Cells and Mitochondria. Biochemistry. 2012; 51:5276–5284. [PubMed: 22726227]
- 29. Whitnall M, Rahmanto YS, Huang MLH, Saletta F, Lok HC, Gutiérrez L, Lázaro FJ, Fleming AJ, Pierre TGS, Mikhael MR. Identification of nonferritin mitochondrial iron deposits in a mouse model of Friedreich ataxia. Proc Natl Acad Sci. 2012
- 30. Stemmler TL, Lesuisse E, Pain D, Dancis A. Frataxin and mitochondrial FeS cluster biogenesis. J Biol Chem. 2010; 285:26737–26743. [PubMed: 20522547]
- 31. Seguin A, Sutak R, Bulteau AL, Garcia-Serres R, Oddou JL, Lefevre S, Santos R, Dancis A, Camadro JM, Latour JM, Lesuisse E. Evidence that yeast frataxin is not an iron storage protein in vivo. Biochim Biophys Acta. 2010; 1802:531–538. [PubMed: 20307653]
- 32. Larrick JW, Cresswell P. Modulation of Cell Surface Iron Transferrin Receptors by Cellular Density and State of Activation. J Supramol Str. 1979; 11:579–586.
- 33. Wiley SE, Rardin MJ, Dixon JE. Localization and function of the 2Fe-2S outer mitochondrial membrane protein MitoNEET. Methods Enzymol. 2009; 456:233–246. [PubMed: 19348892]
- 34. Morales JG, Holmes-Hampton G, Miao R, Guo Y, Münck E, Lindahl PA. Biophysical Characterization of Iron in Mitochondria Isolated from Respiring and Fermenting Yeast. Biochemistry. 2010; 49:5436–5444. [PubMed: 20536189]
- Gohil VM, Sheth SA, Nilsson R, Wojtovich AP, Lee JH, Perocchi F, Chen W, Clish CB, Ayata C, Brookes PS, Mootha VK. Nutrient-sensitized screening for drugs that shift energy metabolism from mitochondrial respiration to glycolysis. Nat Biotechnol. 2010; 28:249–255. [PubMed: 20160716]
- 36. Williams JM, Danson DP, Janot C. A Mössbauer determination of the iron core particle size distribution in ferritin. Phys Med Biol. 1978; 23:835–851. [PubMed: 715001]
- 37. Bovell E, Buckley CE, Chua-anusorn W, Cookson D, Kirby N, Saunders M, St Pierre TG. Dietary iron-loaded rat liver haemosiderin and ferritin: *in situ* measurement of iron core nanoparticle size and cluster structure using anomalous small-angle x-ray scattering. Phys Med Biol. 2009; 54:1209–1221. [PubMed: 19182326]
- 38. Bauminger ER, Harrison P, Nowik I, Treffry A. Composition and dynamics of iron in iron-poor ferritin. Hyperfine Interact. 1988; 42:873–876.
- 39. Miao R, Martinho M, Morales JG, Kim H, Ellis A, Lill R, Hendrich MP, Münck E, Lindahl PA. EPR and Mössbauer Spectroscopy of Intact Mitochondria Isolated from Yah1p-Depleted *Saccharomyces cerevisiae*. Biochemistry. 2008; 47:9888–9899. [PubMed: 18717590]
- Miao R, Kim H, Koppolu MK, Ellis A, Scott RA, Lindahl PA. Biophysical Characterization of the iron in mitochondria from Atm1p-depleted *Saccharomyces cerevisiae*. Biochemistry. 2009; 48:9556–9568. [PubMed: 19761223]
- 41. Campanella A, Rovelli E, Santambrogio P, Cozzi A, Taroni F, Levi S. Mitochondrial ferritin limits oxidative damage regulating mitochondrial iron availability: hypothesis for a protective role in Friedreich ataxia. Hum Mol Genet. 2009; 18:1–11. [PubMed: 18815198]
- 42. Chen W, Paradkar PN, Li L, Pierce EL, Langer NB, Takahashi-Makise N, Hyde BB, Shirihai OS, Ward DM, Kaplan J. Abcb10 physically interacts with mitoferrin-1 (Slc25a37) to enhance its stability and function in the erythroid mitochondria. Proc Natl Acad Sci. 2009; 106:16263–16268. [PubMed: 19805291]
- Paradkar PN, Zumbrennen KB, Paw BH, Ward DM, Kaplan JK. Regulation of Mitochondrial Iron Import through Differential Turnover of Mitoferrin 1 and Mitoferrin 2. Mol Cell Biol. 2009; 29:1007–1016. [PubMed: 19075006]
- 44. Morgan JJ, Surovtsev IV, Lindahl PA. A framework for whole-cell mathematical modeling. J Theor Biol. 2004; 231:581–596. [PubMed: 15488535]

45. Seguin A, Santos R, Pain D, Dancis A, Camadro JM, Lesuisse E. Co-precipitation of phosphate and iron limits mitochondrial phosphate availability in *Saccharomyces cerevisiae* lacking the Yeast Frataxin Homologue (*YFH1*). J Biol Chem. 2011; 286:6071–6079. [PubMed: 21189251]

- 46. Pandolfo M, Pastore A. The pathogenesis of Friedreich ataxia and the structure and function of frataxin. J Neurol. 2009; 256:9–17. [PubMed: 19283345]
- 47. Lu C, Cortopassi G. Frataxin knockdown causes loss of cytoplasmic iron-sulfur cluster functions, redox alterations and induction of heme transcripts. Arch Biochem Biophys. 2007; 457:111–122. [PubMed: 17098208]
- 48. Shaw GC, Cope JJ, Li L, Corson K, Hersey C, Ackermann GE, Gwynn B, Lambert AJ, Wingert RA, Traver D, Trede NS, Barut BA, Zhou Y, Minet E, Donovan A, Brownlie A, Balzan R, Weiss MJ, Peters LL, Kaplan J, Zon LI, Paw B. Mitoferrin is essential for erythroid iron assimilation. Nature Letters. 2006; 440:96–100.
- Nandal A, Ruiz JC, Subramanian P, Ghimire-Rijal S, Sinnamon RA, Stemmler TL, Bruick RK, Philpott CC. Activation of the HIF Prolyl Hydroxylase by the Iron Chaperones PCBP1 and PCBP2. Cell Metabolism. 2011; 14:647–657. [PubMed: 22055506]
- 50. Shi H, Bencze KZ, Stemmler TL, Philpott CC. A Cytosolic Iron Chaperone That Delivers Iron to Ferritin. Science. 2008; 320:1207–1209. [PubMed: 18511687]
- 51. Rothen A. Ferritin and Apoferritin in the ultracentrifuge. J Biol Chem. 1944; 152:679–693.
- 52. Dickson DPE, Reid NMK, Mann S, Wade VJ, Ward RJ, Peters TJ. Mössbauer spectroscopy, electron microscopy and electron diffraction studies of the iron cores in various human and animal haemosiderins. Biochim Biophys Acta. 1988; 957:81–90. [PubMed: 3179322]
- 53. Macara IG, Hoy TG, Harrison PM. The formation of ferritin from apoferritin: kinetics and mechanism of iron uptake. Biochem J. 1972; 126:151–162. [PubMed: 5075227]
- 54. Crichton RR, Paques E. A kinetic study of the mechanism of ferritin formation. Biochem Soc Trans. 1977; 5:1130–1131. [PubMed: 913802]
- 55. St Pierre TG, Tran KC, Webb J, Macey DJ, Pootrakul P, Dickson DPE. Core structures of haemosiderins deposited in various organs in β-thalassemia/Haemoglobin E disease. Hyperfine Interact. 1992; 71:1279–1282.
- 56. Bell SH, Weir MP, Dickson DPE, Gibson JF, Sharp GA, Peters TJ. Mössbauer spectroscopic studies of human haemosiderin and ferritin. Biochim Biophys Acta. 1984; 787:227–236. [PubMed: 6733119]
- 57. Michel FM, Hosein HA, Hausner DB, Debnath S, Parise JB, Strongin DR. Reactivity of ferritin and the structure of ferritin-derived ferrihydrite. Biochim Biophys Acta. 2010; 1800:871–885. [PubMed: 20510340]
- 58. Hartwig A, Schlepegrell R. Induction of oxidative DNA damage by ferric iron in mammalian cells. Carcinogenesis. 1995; 16:3009. [PubMed: 8603477]
- Hartwig A, Klyszcz-Nasko H, Schlepegrell R, Beyersmann D. Cellular damage by ferric nitrilotriacetate and ferric citrate in V79 cells: interrelationship between lipid peroxidation, DNA strand breaks and sister chromatid exchanges. Carcinogenesis. 1993; 14:107–112. [PubMed: 8425256]
- Ingraham, LL.; Meyer, DL. Biochemistry of Dioxygen. 1st. Plenum Press; NY: 1985. Catalases and Peroxidases; p. 91-105.
- 61. Ames BN, Shigenaga MK, Hagen TM. Oxidants, antioxidants, and the degenerative diseases of aging. Proc Natl Acad Sci. 1993; 90:7915–7922. [PubMed: 8367443]
- 62. Cockrell AL, Holmes-Hampton GP, McCormick SP, Chakrabarti M, Lindahl PA. Mössbauer and EPR Study of Iron in Vacuoles from Fermenting *Saccharomyces cerevisiae*. Biochemistry. 2011; 50:10275–10283. [PubMed: 22047049]

#### **Abbreviations**

BPS bathophenanthroline sulfonate
CD central quadrupole doublet

**DFO** desferrioxamine

**DDDI** double-distilled and deionized **DMT1** divalent metal transporter 1

δ isomer shift

 $\Delta E_Q$  quadruple splitting DT doubling time

ECAR extracellular acidification rate

EDTA ethylenediaminetetraacetic acid

EDX Energy dispersive X-ray
EM electron microscopy

**EPR** electron paramagnetic resonance

**FC** ferric citrate

Fecell overall cellular Fe

Fe<sub>c</sub> cytosolic Fe

Fef ferritin-bound Fe

**Fe**<sub>m</sub> mitochondrial Fe, except for Fe found as nanoparticles

 ${\bf Fe_{mo}}$  nanoparticles found in mitochondria

Fe<sub>n</sub> cytosolic nanoparticles Fe

Fe<sub>s</sub> sensed Fe

**HAADF** high-angle-annular-dark-field

**HS** high spin

**IRP1 and IRP2** iron responsive element binding proteins 1 and 2

LS low-spin
MB Mössbauer

MIB mitochondria isolation buffer

**NHHS** nonheme high spin

NTBI nontransferrin-bound iron
OCR oxygen consumption rate
ODE ordinary differential equation
PBS phosphate-buffered saline

**Reg.** surrogate for regulation in which increasing  $Fe_s$  inhibits  $Reg_+$  surrogate for regulation in which decreasing  $Fe_s$  stimulates

**ROS** reactive oxygen species

**STEM** scanning tunneling electron microscopy

TBI transferrin-bound iron
TfRC1 transferrin receptor 1

TfRC<sup>+</sup> cells genetically modified to overexpress TfRC1

UTR untranslated region

**UV-vis** electronic absorption spectroscopy

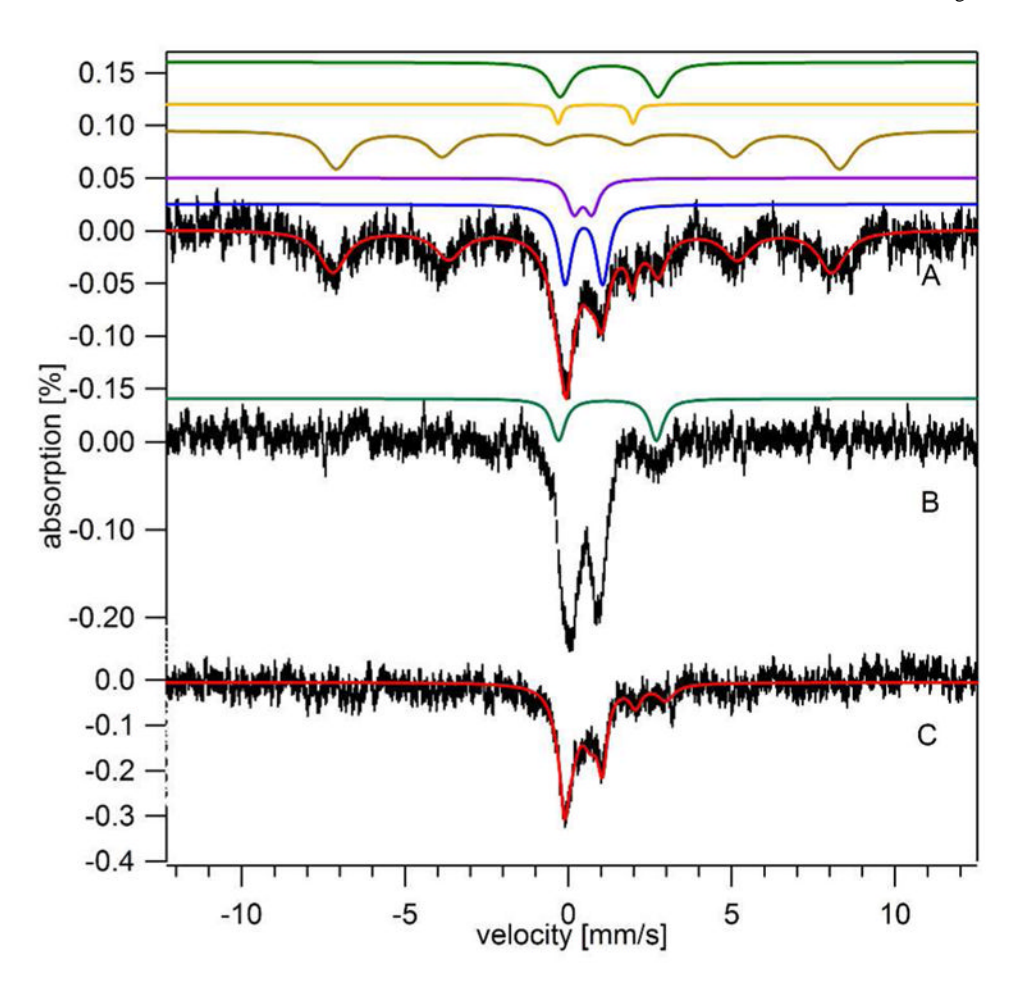


Figure 1. Mössbauer spectra of Jurkat cells grown in medium supplemented with 3  $\mu M$   $^{57}Fe^{III}$  citrate

A, 3  $\mu M$  FC at 5K, 0.05 T; B, same as A but at 70 K. Simulations are as follows: CD (blue,  $\delta=0.46$  mm/s;  $\Delta E_Q=1.2$  mm/s),  $Fe^{III}$  oxyhydroxide nanoparticles (purple,  $\delta=0.48$  mm/s and  $\Delta E_Q=0.57$  mm/s), ferritin (brown,  $\delta=0.54$  mm/s;  $\Delta E_Q=0.20$  mm/s;  $H_{eff}=480$  kG), HS  $Fe^{II}$  hemes (orange,  $\Delta=1.0$  mm/s;  $\Delta E_Q=2.0$  mm/s), and NHHS  $Fe^{II}$  (green,  $\delta=1.3$  mm/s;  $\Delta E_Q=3.0$  mm/s) C, 5 K, 0.05 T MB spectrum of isolated mitochondria from cells grown with 3  $\mu M$  FC. Total simulations for A and C are shown in red.

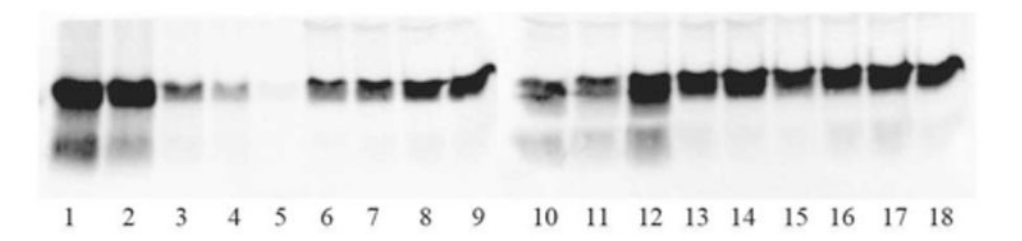


Figure 2. Quantitative Western Blot of ferritin in cell lysates

The lanes given in parentheses were loaded with (1) 1000, (2) 500, (3) 100, (4) 50 and (5) 10 ng of holo-ferritin. The following lanes were loaded with 10  $\mu$ L of lysates: (6) 3FU, (7) 10FU, (8) 30FU, (9) 100FU, (10) 3FL, (11) 10 FL, (12) 30FL, (13) 3TU, (14) 10TU, (15) 30TU, (16) 3TU TfRC<sup>+</sup>, (17) 10TU TfRC<sup>+</sup>, (18) 30TU TfRC<sup>+</sup>.

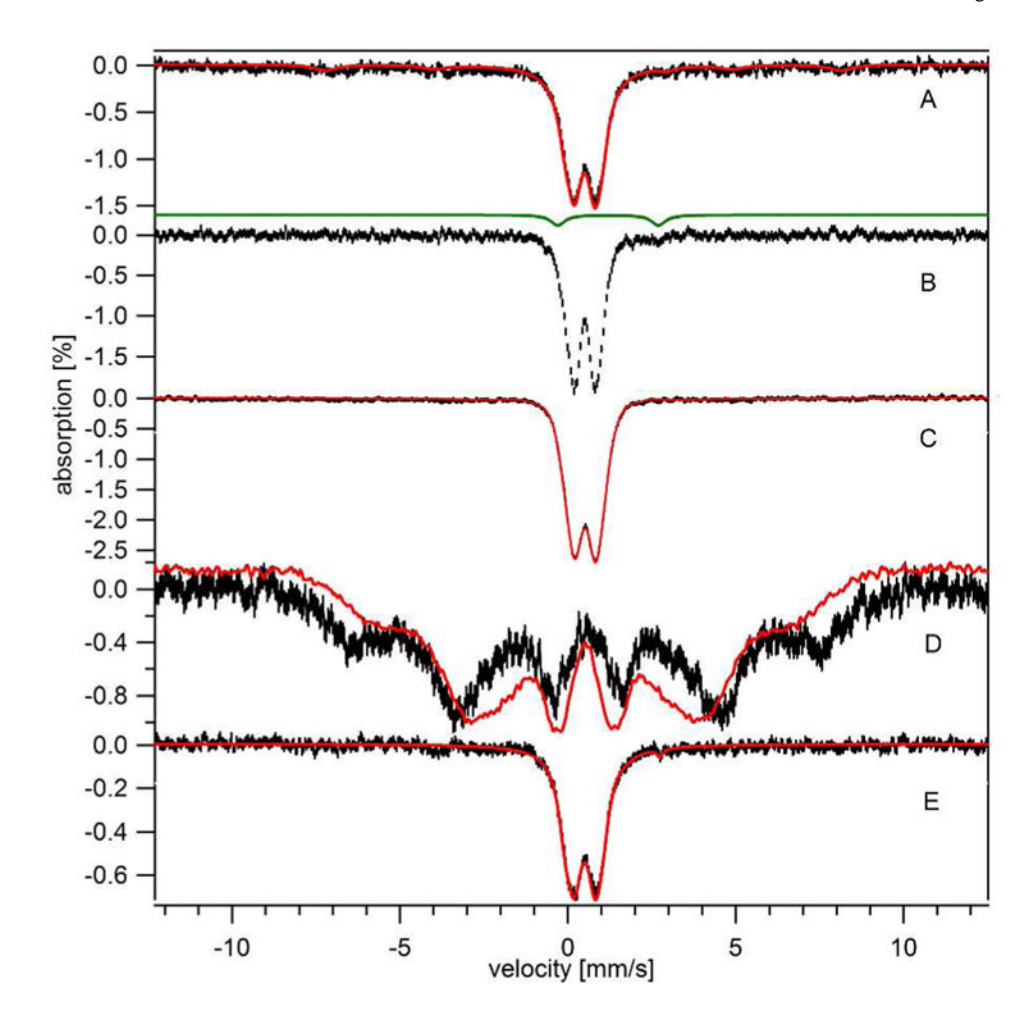


Figure 3. Mössbauer spectra of high-Fe Jurkat cells and mitochondria A, 30FU, 5K, 0.05T; B, 30FU, 70K, 0.05T; C, 100FU, 5K, 0.05T; D, 100FU, 4.3K, 6T, overlaid with a 6T, 4.3 K spectrum (red) of yeast mitochondria isolated from Aft1-1  $^{up}$  cells;  $^{62}$  E, 5K, 0.05T spectrum of mitochondria isolated from cells grown on glucose with 30  $\mu$ M FC. Overall simulations for A and D are shown in red.

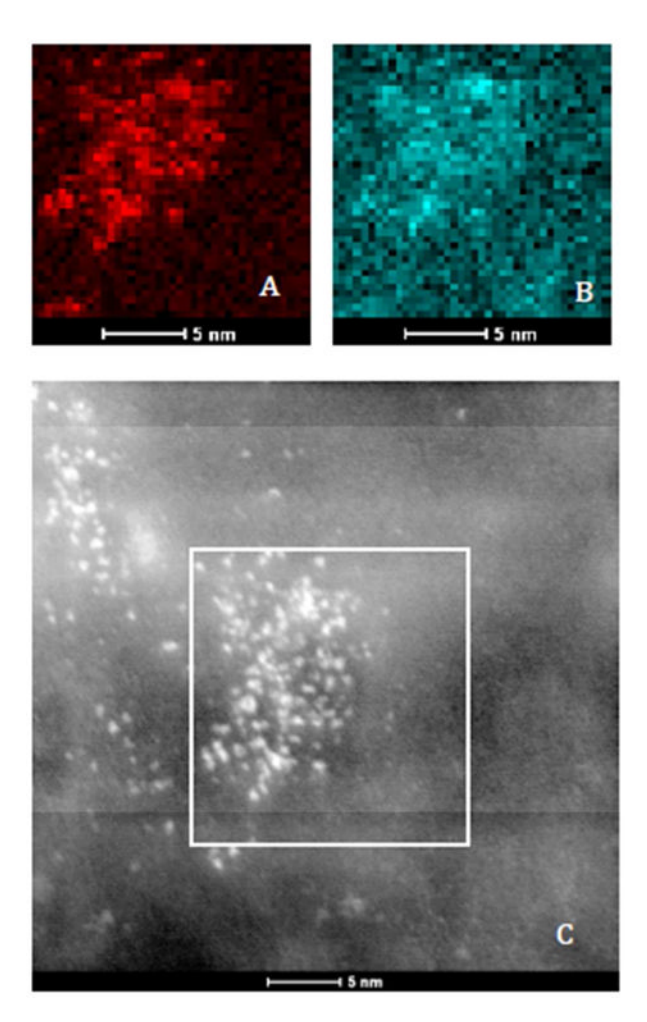


Figure 4. EDX images of glucose-grown cells in medium containing 30  $\mu$ M FC A, Fe map; B, P map; C, 320K magnified image of Fe deposits. The box in C indicates the region in which the elemental maps were obtained.

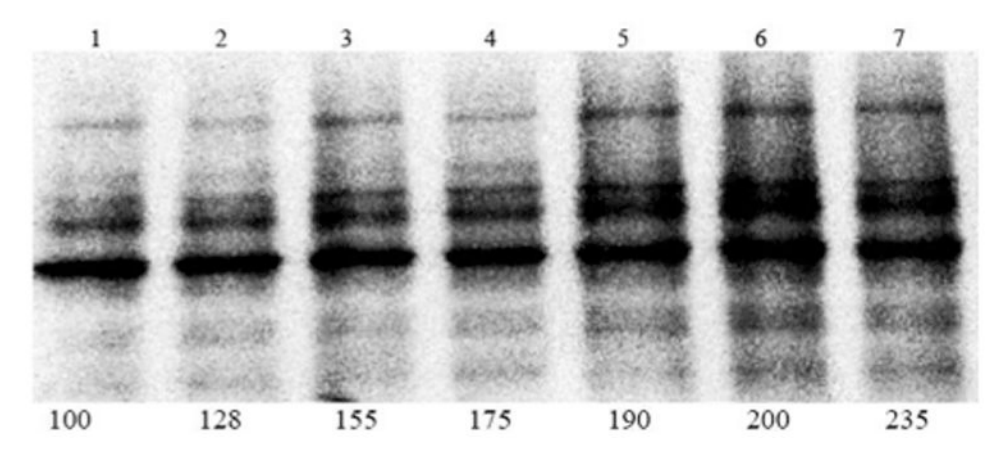
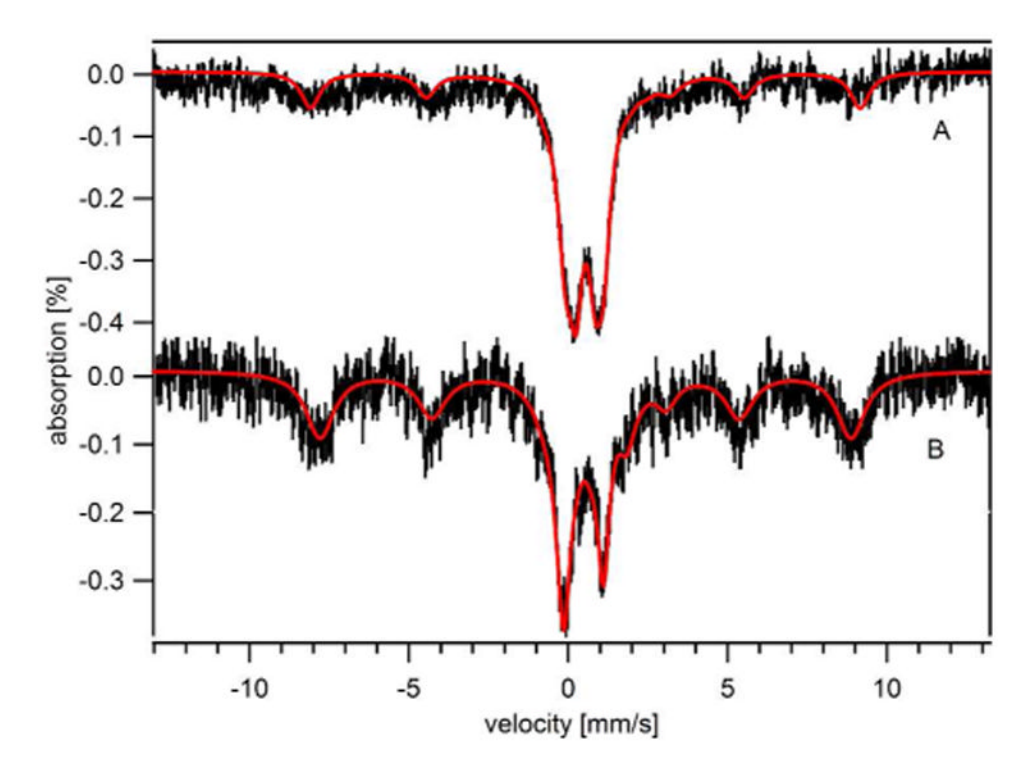
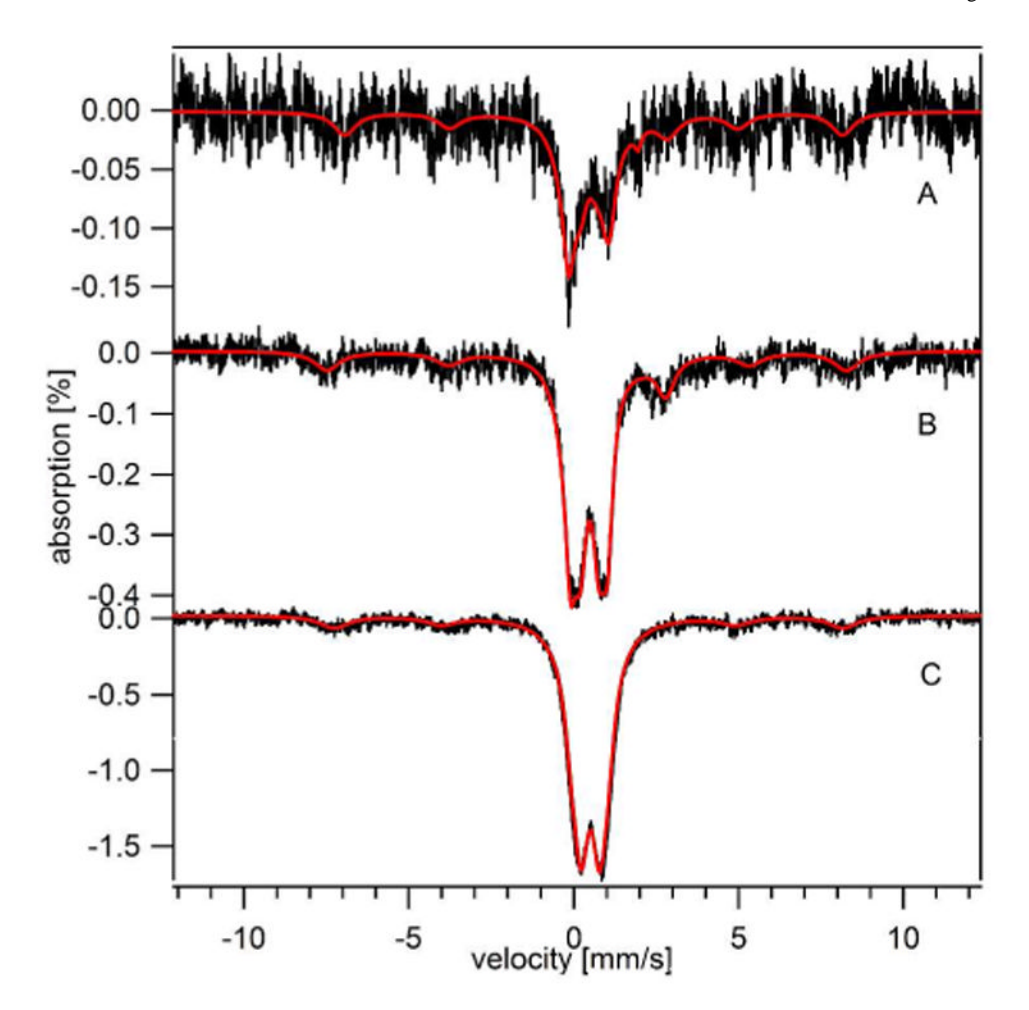


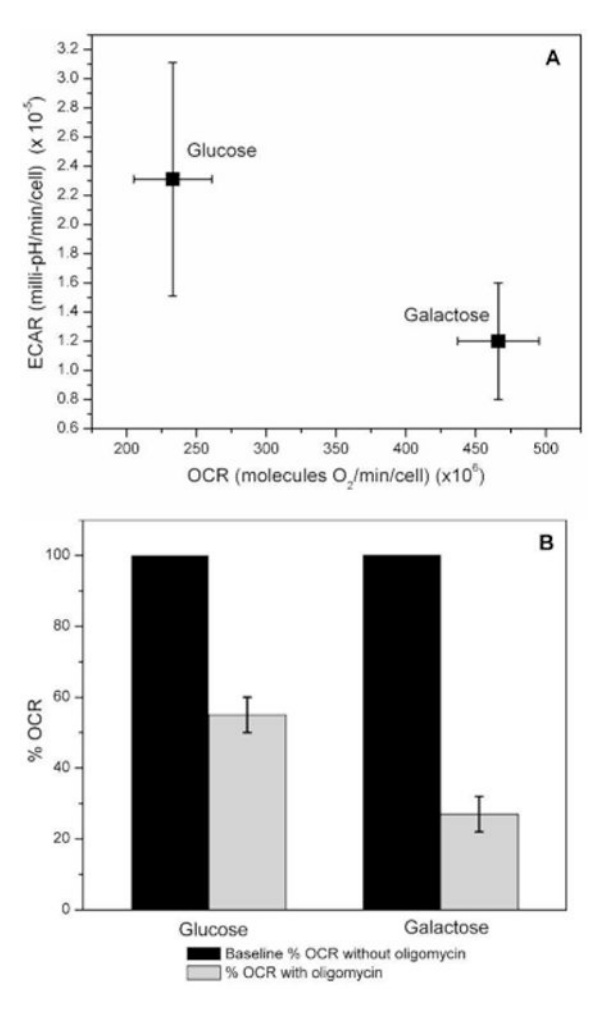
Figure 5. Oxyblot analysis of cells grown under different conditions
Samples include (with lanes in parentheses) (1) 3FU; (2) 10FU; (3) 30FU; (4) 100FU; (5)
3FL; (6) 10FL; (7) 30FL. Percentages of intensities relative to lane 1 are designated below each lane.



**Figure 6. Bioavailability of nanoparticles**A, 5K, 0.05T MB spectra of 20FU cells (half-filled cup); B, derived from A but after washing and further growth on medium unsupplemented with <sup>57</sup>Fe (filled cup).



**Figure 7. 5K, 0.05T Mössbauer spectra of galactose-grown cells** A, 3FL; B, 10FL; and C, 30FL. Simulations are shown in red.



Figure~8.~Oxygen~consumption~rate~(OCR)~and~extracellular~acidification~rate~(ECAR)~of~glucose-~and~galactose-grown~cells

A. Normalized ECAR vs. OCR measurements of cells grown in glucose or galactose. B. Normalized OCR measurements of cells grown in glucose or galactose in the absence (black) or presence (grey) of 1  $\mu$ M oligomycin.

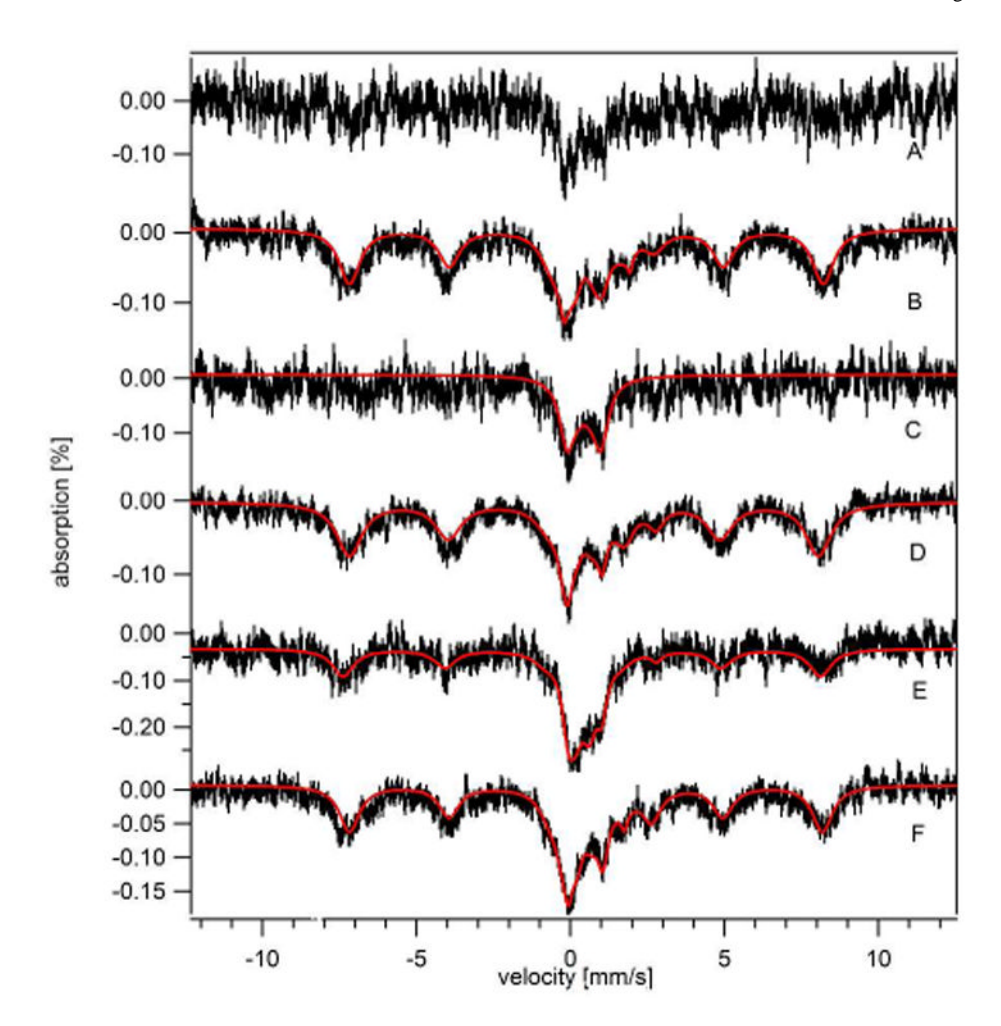


Figure 9. 5K, 0.05T Mössbauer spectra of Jurkat cells grown on TBI and mitochondria isolated therefrom

A, 3TU WT; B, 30TU WT; C, mitochondria isolated from cells in A; D, 3TU TfRC<sup>+</sup>; E, 10TU TfRC<sup>+</sup>; F, WT cells grown in unsupplemented glucose-containing medium with 100  $\mu$ M DFO, and then transferred to medium containing 3  $\mu$ M <sup>57</sup>TBI. Red lines are overall simulations using percentages given in Table 1 and parameters given in the Figure 1 legend.

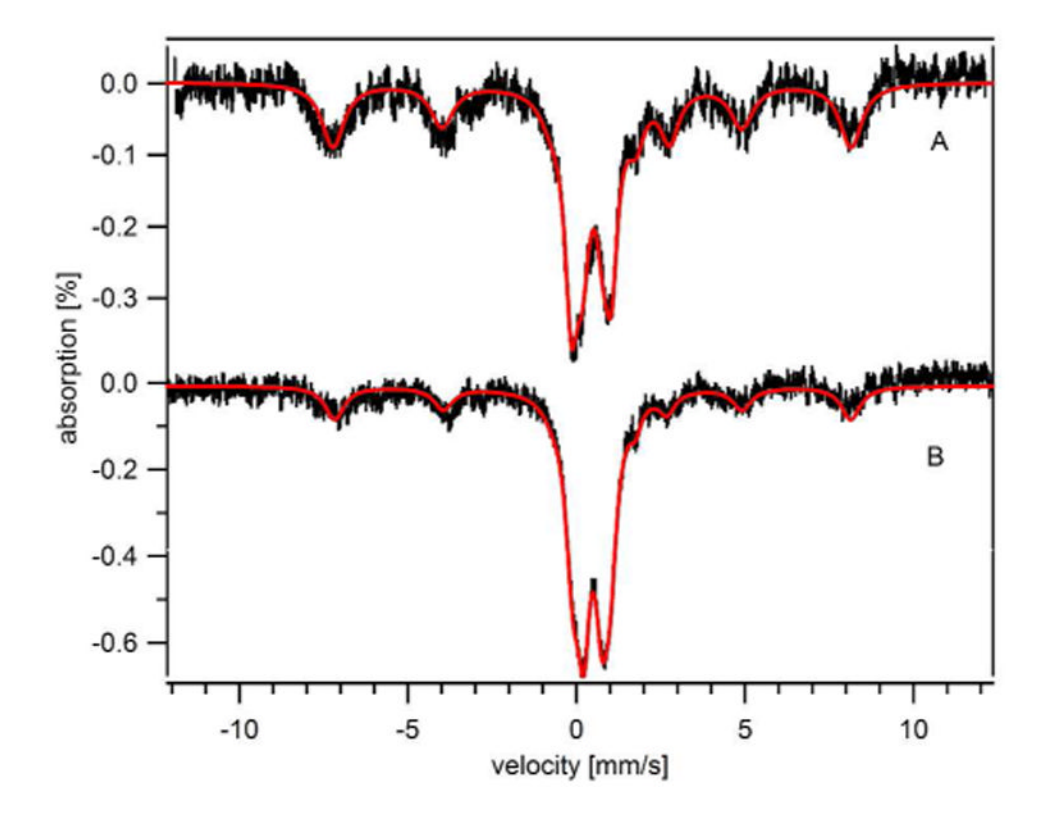


Figure 10. Effect of Frataxin deficiency A, 5K, 0.05T MB spectrum of WT 10FU; B, frataxin-deficient cells grown with 10  $\mu$ M FC. Total simulations are showed in red using percentages given in Table 1.

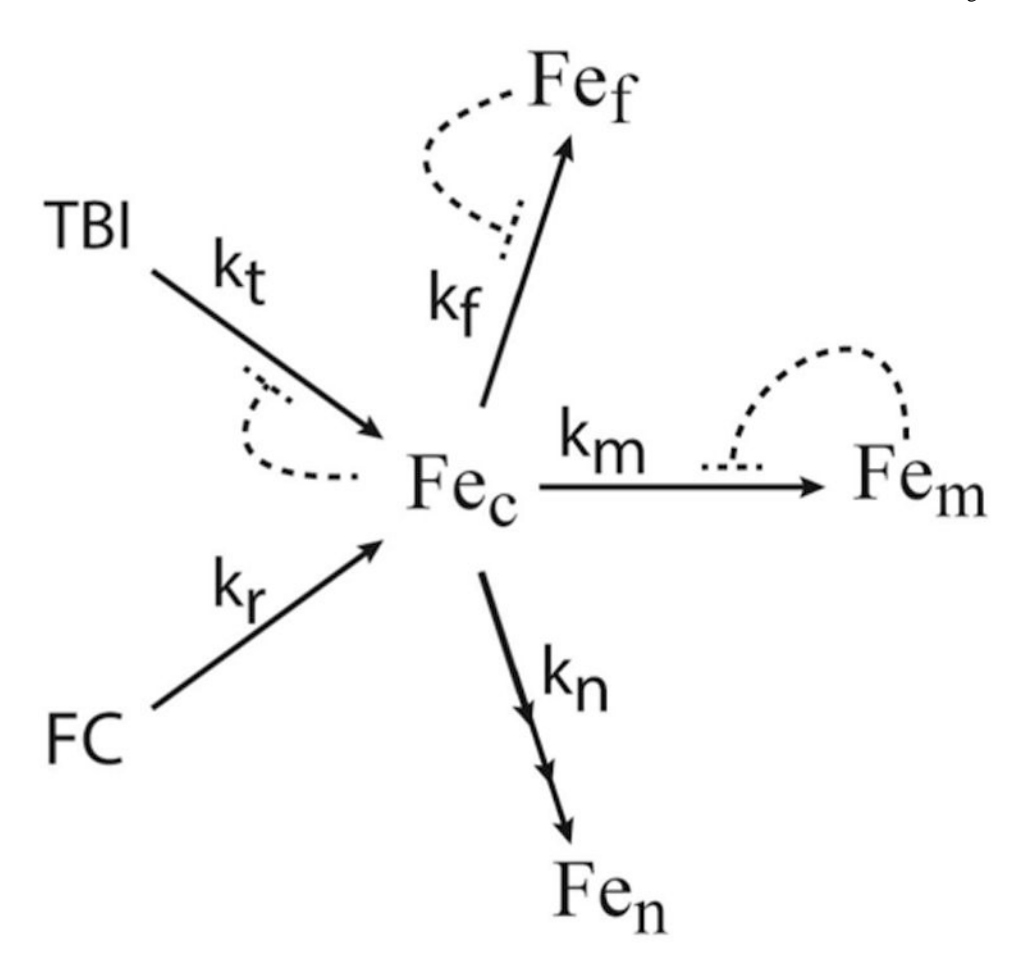


Figure 11. Model of Fe import and intracellular trafficking in Jurkat cells Solid arrows indicate reactions associated with rate-constants  $k_t$ ,  $k_r$ ,  $k_f$ ,  $k_m$  and  $k_n$ . Reactions  $k_t$  and  $k_r$  represent import of TBI and FC Fe, respectively. Reactions  $k_f$  and  $k_m$  represent transfer of Fe<sub>c</sub> to ferritin and mitochondria, respectively. Reaction  $k_n$  represents conversion of cytosolic Fe into nanoparticles. Dashed lines terminating at short straight orthogonal segments represent regulation sites. The lines emanate from the sensed form of Fe. The

triple-headed arrow indicates higher-order dependence of  $Fe_c$  on that reaction.

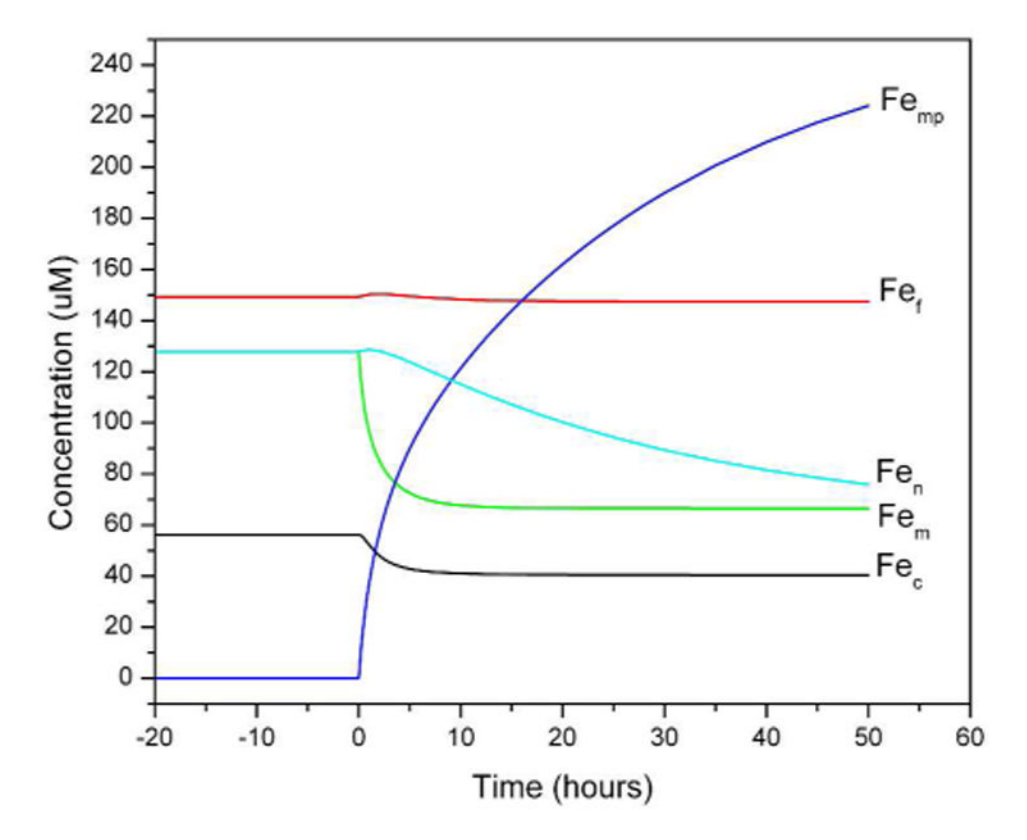


Figure 12. Simulation of the changes in cellular iron distribution following frataxin depletion The simulation at t < 0 is of WT glucose-grown cells in 10  $\mu$ M FC, with DT = 24 hr and  $k_{mp}$  = 0. At t = 0,  $k_{mp}$  was set to 0.000045 hr<sup>-1</sup> and DT to 30 hr.

NIH-PA Author Manuscript

Jhurry et al.

# Table 1

# Iron-related Properties of Jurkat cells

constant  $k_r$  used in the simulation was 1.0 hr<sup>-1</sup>. The cellular Fe concentration was  $220 \pm 65 \,\mu\mathrm{M}$  (average of 3 experiments) while the simulation afforded a WT indicates normal cells, TfRC<sup>+</sup> indicates cells overexpressing TfRC1, and Frxn- indicates frataxin-deficient cells. Replicates n are given in parentheses (1:4), the sample was diluted into medium without Fe supplementation and allowed to grow for 2 doublings. To simulate this, the initial Fe concentrations in the simulation row (38%). Likewise, compare the sum of absolute concentrations (55  $\mu$ M + 11  $\mu$ M = 66  $\mu$ M) in the data row to 82  $\mu$ M in the simulation next 5 columns indicate the percentage of Fe in the sample due to particular groups of Fe centers (based on MB quantification). This is followed, after the comma, by the absolute concentration of that group (obtained by multiplying the percentage by [Fecell]/100). Simulated analogous values are given in the row below. Two of the groups (Fe/S clusters + LS hemes combined with HS Fe<sup>II</sup> hemes) were collectively considered "mitochondrial Fe<sub>m</sub>" by the model. Thus, to compare the data and simulations for this category, add the two percentages in the data row (25% + 5% = 30%) and compare it to the percentage row. In the remaining 4 columns, the experimental and simulated percentages and absolute concentrations can be compared directly. For Frxn cells, the the table. The unusually high value of k, for 3TU "starved" cells suggests that the receptor for FC was also upregulated during the "starving" step of the which  $k_f = 1.8 \text{ hr}^{-1}$ ),  $k_m = 0.27 \text{ hr}^{-1}$ ;  $k_f = 0.55 \text{ hr}^{-1}$ ;  $k_{np} = 0.000045 \,\mu\text{M}^{-1}$ . hr<sup>-1</sup>, and p = 2.9. Uncertainties are given in Table S3. Values for  $k_r$  are given in experiment.  $\alpha = 1/24 \, hr^{-1}$  for all simulations except for 10FL and 30FL, in which case  $\alpha = 1/34 \, hr^{-1}$ , and for Frxn cells where  $\alpha = 1/30 \, hr^{-1}$ . For 20FU concentration of nanoparticles included both cytosol (Fe<sub>n</sub>) and mitochondria (Fe<sub>mp</sub>). Apart from the ferritin protein concentration, data given for 10FU were set to those obtained for 20FU before dilution, and final Fe concentrations were recorded at t = 48 hr. We illustrate how to read the table with the concentration of 216 µM. The concentration of ferritin protein in one of the samples was 0.3 µM, with an average loading of 380 Fe's per ferritin. The simulations,  $K_{Ic} = 9 \mu M$ ; cs = 3;  $K_{Im} = 120 \mu M$ ;  $K_{If} = 130 \mu M$ ;  $k_t = 0.3 \text{ hr}^{-1}$  (except for 3TU "starved" cells for which  $k_t = 3 \text{ hr}^{-1}$  and TfRC<sup>+</sup> cells for row beginning 3FU, WT and the next row labeled "sim". The upper row indicates the data while the lower row indicates the simulation. The overall concentration of FC in the experiment includes the 3 µM Fe that was added to the medium plus 6 µM endogenous Fe. No TBI was added. The ratewhere applicable. The concentration of endogenous Fe was assumed to be 4-6 µM, and was added to the concentration of ferric citrate. For all

Sample	[FC] (µM)	[TBI] (μM)	$k_r$ (hr <sup>-1</sup> )	$[\mathrm{Fe}_{\mathrm{cell}}](n)$	[Ferritin Protein], Fe/Ferritin	Fe/S+LS Hemes %, μΜ	HS Fe <sup>II</sup> hemes %, μΜ	Ferritin [Fe <sub>f</sub> ] %, µM	NHHS Fe <sup>II</sup> [Fe <sub>c</sub> ] %, μM	Nanoparticles [Fe <sub>n</sub> ] %, µM
OU, WT	9 = 9 + 0	0		$100 \pm 3 (I)$				-		-
sim	4	0	8.0	105		31, 3	31, 33= [Fe <sub>m</sub> ]	64,67	5,5	0,0
3FU, WT	3 + 6 = 9	0		$220 \pm 65 (3)$	0.3, 380	25,55	5,11	52,114	13,29	5,11
sim	6	0	1.0	216		3	38, 82	55,119	13,6	1,2
10FU, WT	10 + 6 = 16	0		400±70 (5)	0.3, 530	27,108	4,16	40,160	11,44	18,72
sim	16	0	1.0	384		3.	32,124	38,146	12,45	18,69
30FU, WT	30 + 6 = 36	0		840±276 (3)	0.4, 275	13,109	2,17	13,109	7,60	65,546
sim	36	0	1.0	865		1,	16,135	18,157	10,89	56,483

were reported previously.26

Jhurry et al.

k	$k_r$ (hr <sup>-1</sup> ) [Fe <sub>cell</sub> ] (n)	-	. Fe/Ferritin	Fe/S+LS Hemes %, µM	HS Fe <sup>II</sup> hemes %, μΜ	Ferritin [Fe <sub>f</sub> ] %, µM	NHHS Fe <sup>II</sup> [Fe <sub>c</sub> ] %, μΜ	Nanoparticles [Fe <sub>n</sub> ] %, µM
3700±200 (2)	$\simeq$		0.5,	5,185	:		1	93,3440
1.3 3307				4,	4,144	5,167	5,163	86,2833
142±24 (3)	(3)		0.6,95	40,57	,	40,57	,	,
1.1				37	32,46	63,92	5,7	0,0
160±20 (2)	)		0.8,80	40,64		40,64		
1.1				35	33,56	61,104	5,9	0,1
225±25 (3)			0.4,300	30,68	2,5	54,122	8,18	6,14
1.1 209				37,	37,78	56,117	6,12	1,2
130±6 (2)			0.4,115	35,46	2,3	35,46	11,14	14,18
0.8	i			36	39,86	56,121	5,10	0,1
580±160 (2)			0.4,290	26,151	2,12	20,116	13,75	38,220
1.1 598				23	23,135	26,157	10,62	41,244
2000±300 (2)			1.2,167	10,200	,	10,200	,	79,1580
1.3 1591				9,	9,143	10,165	7,107	74,1176
400±29 (2)	$\sim$ 1		0.5,480	25,100	3,12	60,240	6,24	2,8
1.2 302				38	38,115	46,138	10,29	7,20
510±14 (2)			0.7,290	25,127	2,10	40,204	3,15	30,153
1.0 528				25	25,130	29,151	12,63	35,183
675±33 (2)		(2)		20,135	2,14	20,135	4,27	45,304
1.1 686				19	19,133	22,154	11,77	47,322
225±8 (I)		(J)		37,83	2,5	45,90	10,23	3,7
1.1				3(	30,69	45,104	3,8	21,48
330±5 (1)		(I)	-	19,63	2,7	50,165	16,53	13,43
2.6 328				36	36,119	43,141	11,35	9,31
550±36 (2)		(2)	-	28,154	3,17	20,110	5,28	40,220
1.1 528	ı ~ I			12	12,64	27,146	7,37	53,281

Page 39